Ocean Engineering 348 (2026) 124018

Contents lists available at ScienceDirect

Ocean Engineering

journal homepage: www.elsevier.com/locate/oceaneng

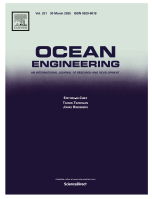

Research paper

Hydroelastic analysis of flexible asymmetric water entry of wedge-shaped bodies using a fully coupled partitioned CFD-CSD model

Sasan Tavakoli [a,b,*], Saeed Hosseinzadeh [c], Theodosis D. Tsaousis [d], Spyros Hirdaris [e]

[a] Australian Maritime College, University of Tasmania, Newnham, Launceston, TAS 7250, Australia
[b] Department of Infrastructure Engineering, The University of Melbourne, Parkville, VIC 3052, Australia
[c] Maritime Engineering, School of Engineering, University of Southampton, Boldrewood Innovation Campus, Southampton, SO16 7QF, UK
[d] School of Naval Architecture and Marine Engineering, National Technical University of Athens, Athens, 15773, Greece
[e] Global Ship Systems Centre, American Bureau of Shipping, Athens, Greece

ARTICLE INFO

Keywords:
Flexible fluid-structure interactions
Water entry
Slamming
Wedge section
Sea loads

ABSTRACT

The asymmetric water entry of a flexible wedge, as an important engineering problem with applications in structural design of hull girder and fatigue life assessment, is studied using an open-source computational code that solves the hydrostructural response of the section entering water using a partitioned approach via a tightly coupled two-way flexible fluid-solid interaction algorithm. Three different simulation campaigns are conducted to provide an understanding of the problem from scientific and engineering perspectives. By running the code for various cases, it is shown that the kinematics of the spray flow on both sides of an asymmetric flexible wedge differ from those of a symmetric wedge with a similar local deadrise angle. It is found that the spray root is decelerated on the heeled-down side and accelerated on the heeled-up side, and this behaviour is found to be proportional to the changes in pressure resulting from the asymmetric flow pattern, as compared to a symmetric condition. It is also demonstrated that the pressure acting on a flexible asymmetric section differs from that on a rigid asymmetric section, with the flexible case showing a reduction in pressure. This reduction is observed to be proportional to the maximum deflection in emerging in the flexible panels of the section entering the water, effectively quantifying both the loss of energy in the water impact and the local geometric changes of the section. Finally, by simulating different heel angles for both flexible and rigid sections, it is shown that the forces and moments acting on the body during water entry exhibit nonlinear behaviour as a function of heel angle, with the nonlinearity becoming more significant as the structure becomes more flexible. The results of this study highlight the importance of considering asymmetric flexible water entry in the design of ships and in the assessment of their safety under large hydrodynamic loads. Such analyses are preferably carried out using models that capture the nonlinearities associated with the fluid flow.

1. Introduction

Water entry has long stood as one of the most interesting free-surface flow phenomena, drawing the attention of naval architects (Hirdaris et al., 2014) and fluid dynamicists alike (Jung, 2025). In practical naval-engineering applications, it arises when ships and high-speed craft interact with incident waves (Kapsenberg, 2011). It happens when the bow, stern, or sections along the hull, often within the forward 30% of the length of the vessel, exit the water, and then again enter into it, followed by a large hydrodynamic force known as the slamming force (Wang and Soares, 2017).

The solution of the water entry problem provides both the hydrodynamic force and the pressure acting on the impacted surface. The former is used for evaluating the transient loads responsible for whipping motions and for performing hydroelastic analysis of the hull girder (Kim et al., 2015). The latter defines the design pressure used in the scantling of structural elements, including hull panels, primary supporting members (PSMs), and stiffeners (Bureau Veritas Marine & Offshore, 2025), and apart from that, it can be used for studying ultimate hull strength and fatigue analysis (Silva and Ravichandran, 2012). Moreover, the hydrodynamic force can be utilised to determine sectional loads in high-speed planing craft, particularly when employing a 2D+t model to simulate the motions of a planing vessel advancing in waves (Zarnick, 1978; Tavakoli et al., 2020; Hosseinzadeh et al., 2019; Tavakoli et al., 2026) or undergoing manoeuvres (Tavakoli and Dashtimanesh (2019), Hosseini et al. (2024)).

* Corresponding author.
E-mail addresses: sasan.tavakoli@utas.edu.au (S. Tavakoli), s.hosseinzadeh@soton.ac.uk (S. Hosseinzadeh), thtsaousis@naval.ntua.gr (T.D. Tsaousis), shirdaris@eagle.org (S. Hirdaris).

https://doi.org/10.1016/j.oceaneng.2025.124018
Received 27 September 2025; Received in revised form 5 December 2025; Accepted 15 December 2025
Available online 29 December 2025

Water entry modelling traces back nearly a century to foundational scholarly studies conducted in the 1920s and 1930s by von Kármán (1929) and Wagner (1932), whose primary aim was to estimate the hydrodynamic loads acting on seaplanes during landing and ditching, under the assumption of rigid body motion. The von Kármán model was based on the principle of momentum variation as a body enters the water. Wagner's model, however, was more advanced. It provided a theoretical solution for the water entry of a rigid body into an inviscid fluid domain, using a flat disc approximation. It was theoretically demonstrated that, for non-flat bodies, a water rise along the wall, referred to as the spray root, emerges during impact. This spray root carries a significant amount of energy and momentum (Panciroli et al., 2015) and is likely the dominant contributor to the hydrodynamic impact force. The formation of the spray root has been confirmed through experiments (Kikuhara, 1960; Greenhow, 1987; Watanabe, 1986; Wilson, 1989), which show that when the spray root reaches a point on the wedge wall, a sharp rise in pressure occurs, followed by a sudden drop as the spray continues to propagate forward (Alaoui et al., 2015; Izadi et al., 2018b; Peseux et al., 2005).

Following the early observations on the physics of water entry, considerable efforts have been devoted to further developing the associated models, with particular emphasis on capturing the nonlinearity of the free surface (Fontaine and Cointe, 1992; Korobkin, 2007), especially the formation of the spray root, and on extending the models to three-dimensional configurations (Scolan and Korobkin, 2001) or wave impact on the structures on the path of steep waves (e.g. in Tsaousis et al. (2020)). This would mostly lead to more accurate predictions of the impact force. These developments have employed analytical modelling (Semenov and Iafrati, 2006; Hascoët et al., 2019), panel methods (Battistin and Iafrati, 2003; Zhao and Faltinsen, 1993; Zhao et al., 1996; Sun et al., 2020), and Computational Fluid Dynamics (CFD) (Facci et al., 2015; Xiang et al., 2020; Wang et al., 2021). The first two approaches are typically based on an inviscid fluid assumption, whereas CFD models are formulated under the assumption of a viscous fluid.

Several models have also investigated the structural side of the problem, focusing on the deformation arising within the structure. These models have been developed in response to the need to look into the structural effects of the water entry on the stresses and strains emerging in the panel subjected to the impact load.

According to Khabakhpasheva and Korobkin (2013), early efforts in this area were undertaken by Weining (1936) and Povitsky (1935) in the 1930s, who employed a quasi-static approach. This method requires the pressure distribution acting on the structure, typically applied over the contact region, while neglecting structural dynamics and fluid–structure interaction effects. In the context of naval architecture, this is often referred to as quasi-static response analysis and has been extensively studied by the Quasi-Static Response Committee of the ISSC (Underwood et al. (2022)). A clear definition of the quasi-static model for water entry is presented in Feng et al. (2021)

Any fluid dynamic model, from linear ones to fully nonlinear ones, may be used to compute the pressure distribution, and various structural solvers, ranging from simple to highly nonlinear models, can be employed to evaluate the instantaneous structural response under a quasi-static approach. Invoking a quasi-static model, however, requires a deep understanding of the dynamic effects, which are measured by the ratio between the elastic response of the structure and the loading period (i.e., the time duration over which the impact occurs) (Datta and Siddiqui, 2016; Stenius et al., 2007).

From a technical standpoint, this involves the interplay between the lowest natural frequency of the structure and the impact duration. If the latter is significantly longer than the characteristic period associated with the natural frequency, the response is likely to be dominated by static effects (e.g. in Datta and Siddiqui (2016)). This behaviour has been observed and discussed in several theoretical and numerical studies (Vasin, 1993; Datta and Troesch, 2012). However, the present research does not aim to investigate this aspect in detail, which should be covered in a separate study.

Dynamic response analysis, on the other hand, directly examines the hydroelastic (or so-called hydrostructural) responses of a body entering water. This approach accounts for dynamic effects and may also incorporate the mutual interaction between the fluid and solid domains during the water entry process. Dynamic effects may lead to reduced displacement in the impacted structure under relatively low-impact conditions (Datta and Siddiqui, 2016; Stenius et al., 2007). However, they may intensify the response when the period corresponding to the lowest natural frequency of the structure closely matches the duration of the impact. That is, when resonance occurs, a dynamic response analysis gives a greater response than what is predicted by static analysis. This aspect is not explored in the present study.

Hydroelastic effects can influence not only the structural response but also the surrounding fluid field. As the spray root forms along the wall of the structure, part of its momentum is transferred to the structure, causing deflection. Consequently, the energy of the spray, responsible for generating hydrodynamic pressure and loading, is partially transferred to the solid body, reducing the immediate impact force (e.g. in Tavakoli et al. (2023a), Yan et al. (2023)). However, as water detachment occurs (water separation for wedge section bodies), a whipping response emerges, wherein the structure releases part of the absorbed momentum back into the surrounding fluid. This interaction may continue until the structure reaches a dynamic equilibrium. But simply, during the early stage of impact, the force and pressure experienced by a flexible structure are reduced compared to those experienced in a rigid body impact. This has also been seen during the flat plate water entry processes (e.g. in Mai et al. (2020), Yan et al. (2021, 2022)).

Considering hydroelasticity and the dynamic responses that emerge during the water entry process requires solving the water entry problem using a flexible fluid–structure interaction (FFSI) modelling approach. This involves coupling the fluid and solid sub-problems. The fluid domain may be idealised using any of the established models, ranging from analytical formulations to CFD-based approaches; similarly, various modelling strategies can be employed for the solid domain, such as Computational Solid Dynamics (CSD). However, in such cases, a well-defined fluid–solid interface is required, through which a momentum balance must be enforced. In a broader view, within the ocean engineering and naval architecture community, various approaches and algorithms have been developed for solving FFSI problems, each associated with its own sources of uncertainty (Amouzadrad et al. (2025)).

The earliest FFSI model was developed by Meyerhoff (1965), based on a dry beam idealisation and employing the water entry model of Wagner (1932). Subsequently, a similar approach was adopted by Vasin (1993), who extended the formulation for hydroelastic water entry. Since then, a variety of different models for flexible water entry have been developed. Some models have developed for solving flat horizontal, flexible-bottom water entry problems (Faltinsen et al., 1997; Kvalsvold and Faltinsen, 1993, 1994; Wang et al., 2016), either two-dimensional or three-dimensional, while others have built to model non-horizontal flat flexible structures entering water, such as trimmed plates (representing, for instance, the deck of a catamaran or the bottom structure of a seaplane) or wedge-shaped sections (Khabakhpasheva and Korobkin (2013), Hosseinzadeh and Tabri (2021)). In several of these models, the trimmed plate is also considered under oblique impact conditions (Izadi et al., 2018a; Hosseinzadeh et al., 2020).

In a series of studies on flexible flat-bottom water entry, it has been demonstrated that the hydroelastic response consists of two distinct stages. The first stage, commonly referred to as the inertia phase, is characterised by a rapid increase in impact force, resulting in significant structural deflection. This is followed by a second stage known as free vibration or so-called whipping, during which the structure oscillates in response to the initial loading. For non-flat flexible structures, this two-stage behaviour may not be as clearly observed (Faltinsen et al., 1997). As discussed earlier, non-flat geometries are subjected to

pressure distributions that propagate either transversely or longitudinally along the structural panel or beam, depending on the configuration. In the case of a wedge entering water, such as the one considered in the present study, the pressure load propagates transversely (Datta and Troesch, 2012; Hosseinzadeh et al., 2023a). In contrast, for a trimmed plate representing, for example, a catamaran deck plate, the load tends to propagate longitudinally (Faltinsen (2000)). This propagation of the load may introduce a phase in between the inertia stage and free vibration, over which strongly coupled fluid-solid interaction may appear. This has been followed by the introduction of more advanced numerical and computational models over time (Wang et al. (2021), Yan et al. (2022), Jiao et al. (2024)).

Regardless of the modelling approach employed to simulate flexible water entry, the problem is incompletely understood from both physical and engineering perspectives. Although remarkable progress has been achieved in modelling symmetric flexible wedges (or other bow sections, such as curved wedges, e.g. in Piro and Maki (2013), Maki et al. (2011), Sun et al. (2024), Moradi et al. (2021), Hosseinzadeh et al. (2023b)), the understanding of more general configurations, particularly asymmetric cases, is still not clear (for a review of recent progress in FFSI modelling water entry problem, refer to Tavakoli et al. (2025)). It is worth noting that asymmetric water entry is, in fact, common in practical scenarios, often occurring when the ship is exposed to oblique seas and beam seas (Chen et al., 2024; Lin et al., 2020; Vijith and Rajendran, 2023; Hosseinzadeh and Tabri, 2024), or even when it manoeuvres (Xu et al., 1998; Judge et al., 2004). If the bow of a ship exits the water, such conditions can induce torsional whipping and horizontal bending responses, phenomena that can not be addressed by a symmetric water entry model, such as that of von Kármán (1929).

For the case of symmetric flexible wedges entering water, structural flexibility significantly influences both fluid and solid motions as mentioned before, and the resulting loads and deflections are strongly dependent on structural rigidity (Tavakoli et al., 2023a; Hosseinzadeh et al., 2023a,b). However, for asymmetric bodies (shown in Fig. 1), the current level of understanding is limited. An asymmetric wedge represents an ideal case for investigating such phenomena, offering a simplified yet representative configuration for studying the effects of asymmetry. The asymmetry in the wedge geometry changes the momentum distribution on either side of the structure relative to the symmetric case. Furthermore, under oblique impact conditions, it may even lead to flow detachment near the apex of the wedge, an effect not addressed in the present study.

The asymmetric flexible wedge water entry problem can, in principle, be studied using any model capable of reconstructing the fluid and solid motions throughout the process. However, due to the limitations of analytical models, which are typically restricted to the early stages of impact and are generally not formulated to capture phenomena such as flow detachment or the subsequent whipping response, a computational approach, solving viscous flow around sections entering water, is adopted in the present study. As such, this paper aims to use a computational model to simulate the water entry of flexible asymmetric wedges, with the objective of providing a deeper understanding of the problem. Specifically, it aims to investigate how asymmetric flow patterns influence the hydrostructural response of a wedge entering water, how structural flexibility affects the hydrodynamics of the entry process, and how increasing heel angle alters the forces acting on the section. Hence, the novelty of this work may be viewed from two complementary perspectives. First, the flexible fluid–structure interaction of a flexible, asymmetric wedge is solved using a fully three-dimensional idealisation of the solid domain. The momentum equation is treated directly, without resorting to beam or shell idealisation (commonly employed in finite-element method, FEM, Tavakoli et al. (2025)). Fluid and solid motions are therefore resolved within a consistent numerical scheme, in contrast to previous Wagner-based, inviscid fluid-based, and CFD-FEM approaches (e.g. Khabakhpasheva and Korobkin (2013), Izadi et al. (2018a), Gilbert et al. (2023)). In addition, the only viscosity-based model in the literature (a CFD–FEM approach, Izadi et al. (2018a)) that addresses the water entry of a flexible wedge is limited to the early stage of the problem, i.e. before water re-attachment. In contrast, the present study solves the problem well beyond the flow-separation stage in order to capture the full whipping response.

Second, the present study provides a new physical understanding of how asymmetric flow conditions influence the water entry process of a flexible wedge. This physical aspect has not been studied previously. By comparing symmetric and asymmetric water entry of flexible wedges under identical local geometric and kinematic conditions, the sole effect of heel-induced asymmetry is isolated, and the resulting changes in the spray-root, pressure evolution, and hydrostructural response of the panel subjected to the slamming load are quantified. Such analysis permits quantifying how panel deflection under an asymmetric condition modifies the local impact pressure. Earlier studies, while limited to symmetric wedges, have related deflection to the non-dimensional ratio of loading period to the lowest natural period (e.g. Gilbert et al. (2023)), whereas herein the change in impact pressure acting on a flexible wedge relative to the impact pressure acting on a rigid wedge, as a baseline, is evaluated directly as a function of panel deflection.

The rest of the present paper is structured as follows. Section 2 presents the governing equations for the fluid and solid domains, along with the boundary conditions applied to various surfaces. Section 3 describes the computational approach used to solve the coupled problem. Section 4 presents the results in three stages to develop a comprehensive understanding of the problem. Finally, Section 5 offers the concluding remarks.

2. Flexible fluid-structure interaction (FFSI) model

A two-dimensional computational domain, shown in Fig. 2, containing an elastic wedge with a half-beam width of b is assumed. The region occupied by the wedge is designated as the solid domain $\mathbf{\Omega}_{\mathrm{S}} \subset \mathbb{R}^2$, and the surrounding region is defined as the fluid domain $\mathbf{\Omega}_{\mathrm{F}} \subset \mathbb{R}^2$. The fluid domain is filled with air-water mixture, they are allowed to be mixed, but they can never react with each other. The fluid and solid domains mutually share boundaries separating them from each other, which is referred to as a fluid-solid interface ($\mathbf{\Gamma}_{\mathrm{FSI}} = \partial\mathbf{\Omega}_{\mathrm{F}} \cap \partial\mathbf{\Omega}_{\mathrm{S}}$). The boundaries of the fluid domain are called fluid boundaries, and are shown with $\mathbf{\Gamma}_{\mathrm{F}} \subset \partial\mathbf{\Omega}_{\mathrm{F}}$. The above assumption gives rise to two distinct physical problems, namely the fluid and the solid. The equations of motion in each domain are solved separately, but they are coupled and balanced at the fluid–solid interface $\mathbf{\Gamma}_{\mathrm{FSI}}$. The computational domain is designed in such a way as to ensure minimal blockage effects. Hence, $\mathbf{\Omega}_{\mathrm{F}}$ is set to extend over a width of $20b^{\bullet}$ (where $2b^{\bullet} = 2b\cos\psi$ is horizontal projection of the beam of a heeled wedge, with ψ denoting the heel angle), and to minimise shallow water effects, $\mathbf{\Omega}_{\mathrm{F}}$ is set to be $24b^{\bullet}$ in height. These dimensions are chosen based on the experience of previous researchers (e.g. in Aagaard (2013), Shi et al. (2025)). The fluid domain, $\mathbf{\Omega}_{\mathrm{F}}$, is filled with water up to a height of approximately $5b^{\bullet}$. The apex of the elastic wedge is initially positioned $\approx 0.04b^{\bullet}$ above the water surface.

To formulate the fluid problem, a right-handed coordinate system is placed at the apex of the wedge. The fluid, as previously stated, is assumed to be viscous and incompressible. The effects of viscosity are expected to manifest primarily following flow separation from the chines of the wedge. The assumption of incompressibility may be justified by the topology of the structure and low Mach number. For a wedge-shaped section, as opposed to a flat-bottomed structure, air entrapment and the resulting air–water mixing near the wall of the structure are anticipated to be minimal. This lends credence to the presumption of an incompressible air–water flow around the section as it enters the water. The problem, as discussed previously, is solved using a coupled CFD–CSD approach. A mesh-based method is employed, which will be introduced in the next section. Accordingly, mesh displacement in the fluid domain, $\mathbf{\Omega}_{\mathrm{F}}$, denoted by $\boldsymbol{w}_{\mathrm{m}}$, must be accounted for in the governing equations.

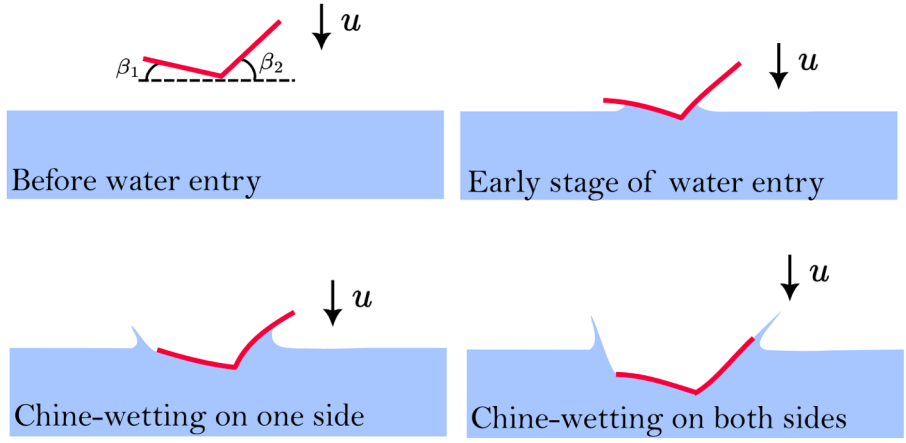

Fig. 1. Water entry of an elastic wedge. This schematic shows different stages, including before the water entry process, the early stage of the impact, chine wetting on one side, and chine wetting on both sides.

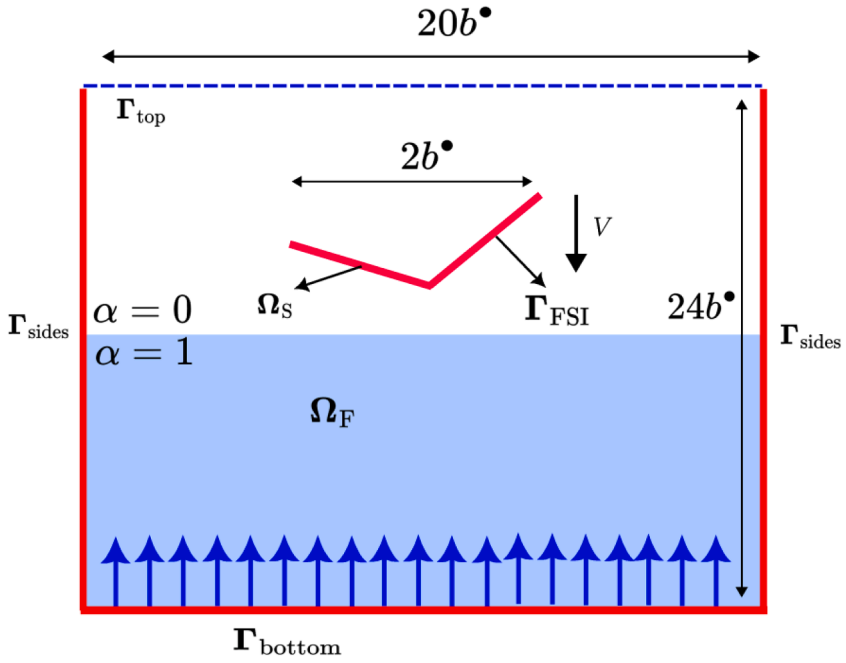

Fig. 2. Sketch of the problem domain showing a flexible, heeled wedge entering the water. The moving-water approach is used (water is driven past a stationary wedge), with zero-shear (slip) boundary conditions applied on the side boundaries.

Time rate of mesh displacement, $\boldsymbol{u}_{\mathrm{m}}$, gives mesh motion as

$$\boldsymbol{u}_{\mathrm{m}} = \frac{\partial \boldsymbol{w}_{\mathrm{m}}}{\partial t}. \tag{1}$$

Hence, the continuity and Navier–Stokes equations govern the fluid domain and are given by

$$\int_{\Omega_{\mathrm{F}}} \nabla \cdot (\boldsymbol{u} - \boldsymbol{u}_{\mathrm{m}})\, dV = 0, \tag{2}$$

$$\int_{\Omega_{\mathrm{F}}} \frac{\partial(\rho_{\mathrm{e}}\boldsymbol{u})}{\partial t}\, dV + \oint_{\Gamma_{\mathrm{F}}} \rho \boldsymbol{u}(\boldsymbol{u} - \boldsymbol{u}_{\mathrm{m}}) \cdot \boldsymbol{n}\, dA = -\oint_{\Gamma_{\mathrm{F}}} p\, \boldsymbol{n}\, dA + \oint_{\Gamma_{\mathrm{F}}} \mu_{\mathrm{e}} (\nabla \boldsymbol{u}) \cdot \boldsymbol{n}\, dA + \int_{\Omega_{\mathrm{F}}} \boldsymbol{f}_{\sigma}\, dV. \tag{3}$$

In the above equations, $\boldsymbol{u}(\boldsymbol{x};t)$ and $p(\boldsymbol{x};t)$ are respectively velocity and pressure fields, which are unknowns and need to be found over time. $\rho_{\mathrm{e}}(\boldsymbol{x};t)$ and $\mu_{\mathrm{e}}(\boldsymbol{x};t)$ are the effective density and effective dynamic viscosity of the fluid, also referred to as mixture density and mixture viscosity. In addition, $\boldsymbol{f}_{\sigma}$ denotes the surface tension force, which arises only at the air–water interface.

The air-water flow is modelled using a two-phase fluid model, for which a Volume of Fluid (VOF) model is employed. As such, a volume fraction field, denoted by $\alpha(\mathbf{x}, t)$, is introduced, which satisfies

$$\int_{\Omega_{\mathrm{F}}} \frac{\partial \alpha}{\partial t}\, dV + \oint_{\Gamma_{\mathrm{F}}} \alpha\, (\boldsymbol{u} - \boldsymbol{u}_{\mathrm{m}}) \cdot \boldsymbol{n}\, dA + \oint_{\Gamma_{\mathrm{F}}} \alpha(1-\alpha)\, \boldsymbol{u}_{c} \cdot \boldsymbol{n}\, dA = 0. \tag{4}$$

Here, $\boldsymbol{u}_{c}$ is the compression velocity of the free surface, which is given by

$$\boldsymbol{u}_{c} = c_{\alpha}\, \min\left(|\boldsymbol{u}|, u_{\mathrm{ref}}\right) \frac{\nabla \alpha}{|\nabla \alpha|}. \tag{5}$$

The surface tension force per unit area is calculated as

$$\boldsymbol{f}_{\sigma} = \gamma\, \kappa\, \nabla \alpha. \tag{6}$$

Here, γ is the surface tension coefficient, and κ is the curvature of the air-water interface, which is given by

$$\kappa = -\nabla \cdot \left(\frac{\nabla \alpha}{|\nabla \alpha|} \right). \tag{7}$$

Using the temporal and spatial values of α across the computational domain, $\mathbf{\Omega}_{\mathrm{F}}$, the effective density and effective dynamic viscosity are calculated by

$$\rho_{\mathrm{e}}(\boldsymbol{x};t) = \alpha \rho_{\mathrm{water}} + (1-\alpha)\rho_{\mathrm{air}}, \tag{8}$$

$$\mu_{\mathrm{e}}(\boldsymbol{x};t) = \alpha \mu_{\mathrm{water}} + (1-\alpha)\mu_{\mathrm{air}}. \tag{9}$$

Finally, mesh motion in $\mathbf{\Omega}_{\mathrm{F}}$ is governed by

$$\int_{\Omega} \nabla \cdot \left(\gamma_d \nabla \boldsymbol{w}_{\mathrm{m}} \right) dV = \mathbf{0}, \tag{10}$$

where γ_d is the diffusivity coefficient.

In the solid domain, the unknown is the displacement field, denoted by $\boldsymbol{w}(\boldsymbol{x};t)$, which is governed by the momentum balance equation, expressed as follows

$$\int_{\mathbf{\Omega}_{\mathrm{S}}} \rho_{\mathrm{S}} \frac{\partial^2 \boldsymbol{w}}{\partial t^2} \, dV = \oint_{\mathbf{\Gamma}_{\mathrm{S}}} \boldsymbol{\sigma}_{\mathrm{S}} \cdot \boldsymbol{n} \, dA + \int_{\mathbf{\Omega}_{\mathrm{S}}} \rho_{\mathrm{S}} \boldsymbol{b} \, dV. \tag{11}$$

Here, ρ_S is the density of the solid body, $\boldsymbol{\sigma}_{\mathrm{S}}$ is the stress tensor, and $\boldsymbol{b}$ represents body forces per unit mass acting within the solid domain.

The displacement in the solid body is assumed to be linear. That is, neither geometric nor material nonlinearities are considered. This assumption holds provided that $||\nabla \boldsymbol{w}|| << 1$. Such an approximation is justified for the water entry of flexible wedges with a Young's modulus exceeding 10^9 Pa, as the maximum wall deflection is expected to remain significantly smaller than the effective beam of the structure (hence, the present model may not be applicable for studying lightweight structures). Under this assumption, the strains developing in the solid body are related to the displacement field as

$$\boldsymbol{\epsilon} = \frac{1}{2}\left(\nabla \boldsymbol{w} + (\nabla \boldsymbol{w})^T \right). \tag{12}$$

The stresses acting on the solid body are linked to strains via Lamé parameters (λ_S and μ_S), as

$$\boldsymbol{\sigma}_{\mathrm{S}} = \lambda_{\mathrm{S}} \, \mathrm{tr}(\boldsymbol{\epsilon}) \, \mathbf{I} + 2\mu_{\mathrm{S}} \, \boldsymbol{\epsilon}. \tag{13}$$

Lame parameters, λ_S and μ_S, are given by

$$\lambda_{\mathrm{S}} = \frac{E\nu}{(1+\nu)(1-2\nu)} \qquad \text{and} \qquad \mu_{\mathrm{S}} = \frac{E}{2(1+\nu)}. \tag{14}$$

Here, E denotes the Young's modulus of the solid body, and ν is the Poisson's ratio.

To model the problem, it is assumed that water moves toward the structure. Accordingly, the following initial condition is imposed in the fluid domain:

$$\boldsymbol{u}(\boldsymbol{x},0) = \boldsymbol{u}_0, \quad p(\boldsymbol{x},0) = 0, \quad \alpha(\boldsymbol{x},0) = H(y_w - y) \quad \forall \boldsymbol{x} \in \mathbf{\Omega}_{\mathrm{F}}, \quad t > 0, \tag{15}$$

where, $\boldsymbol{u}_0 = (0, -u)$ is the initial velocity field in the fluid, and u is the prescribed water entry speed. $H(y_w - y)$ is Heaviside step function, given as

$$H(s) = \begin{cases} 1, & s > 0 \\ 0, & s \le 0. \end{cases} \tag{16}$$

Let $\mathbf{\Gamma}_{\mathrm{inlet}} \subset \partial \mathbf{\Omega}_{\mathrm{F}}$ be the inlet boundary. The condition

$$\boldsymbol{u}(\boldsymbol{x},t) = \boldsymbol{u}_0, \quad \frac{\partial p}{\partial \boldsymbol{n}} = 0, \quad \alpha(\boldsymbol{x},t) = 1 \quad \forall \boldsymbol{x} \in \mathbf{\Gamma}_{\mathrm{inlet}}, \quad t > 0, \tag{17}$$

should be satisfied on this boundary. $\boldsymbol{u}_0$ does not vary over time, which reflects a constant water entry problem.

Let $\mathbf{\Gamma}_{\mathrm{sides}} \subset \partial \mathbf{\Omega}_{\mathrm{F}}$ represent the two side boundaries of the fluid domain. A slip-wall boundary condition should be satisfied on this boundary. Hence, no penetration is permitted (i.e., the normal component of velocity is set to zero), though the tangential component of velocity remains free (i.e., no shear stress is applied). Neumann boundary conditions are imposed for pressure and volume fraction at $\mathbf{\Gamma}_{\mathrm{sides}}$. Mathematically, this can be written as

$$\boldsymbol{u} \cdot \boldsymbol{n} = 0, \quad \frac{\partial \boldsymbol{u}_{\parallel}}{\partial \boldsymbol{n}} = 0, \quad \frac{\partial p}{\partial \boldsymbol{n}} = 0, \quad \frac{\partial \alpha}{\partial \boldsymbol{n}} = 0 \quad \forall \boldsymbol{x} \in \mathbf{\Gamma}_{\mathrm{sides}}, \quad t > 0. \tag{18}$$

Finally, $\mathbf{\Gamma}_{\mathrm{top}} \subset \partial \mathbf{\Omega}_{\mathrm{F}}$ is defined as the top boundary of the fluid domain. This surface represents a free outlet boundary, which is mathematically expressed as

$$\frac{\partial \boldsymbol{u}}{\partial \boldsymbol{n}} = 0, \quad \frac{\partial p}{\partial \boldsymbol{n}} = 0, \quad \frac{\partial \alpha}{\partial \boldsymbol{n}} = 0 \quad \forall \boldsymbol{x} \in \mathbf{\Gamma}_{\mathrm{top}}, \quad t > 0. \tag{19}$$

On the fluid–solid interface ($\mathbf{\Gamma}_{\mathrm{FSI}}$), a balance between the fluid and solid motions must be satisfied. That is, the fluid is neither permitted to penetrate nor to slip along the interface. Accordingly, the normal component of the fluid velocity ($\boldsymbol{u}.\boldsymbol{n}$) must equal the time derivative of the displacement on the solid side of the fluid–solid interface. The pressure on the fluid side of the interface satisfies a Neumann boundary condition, and the displacement on the solid side is computed based on the traction force derived from the fluid-side pressure. As such, the boundary condition governs $\mathbf{\Gamma}_{\mathrm{FSI}}$ can be mathematically written as

$$\boldsymbol{u} \cdot \boldsymbol{n} = \frac{\partial \boldsymbol{w}}{\partial t} \cdot \boldsymbol{n}, \quad \boldsymbol{\sigma}_{\mathrm{S}} \cdot \boldsymbol{n} = \boldsymbol{\sigma}_{\mathrm{F}} \cdot \boldsymbol{n}, \quad \frac{\partial p}{\partial n} = 0, \quad \frac{\partial \alpha}{\partial n} = 0 \quad \forall \boldsymbol{x} \in \mathbf{\Gamma}_{\mathrm{FSI}}, \quad t > 0. \tag{20}$$

Let $\mathbf{\Gamma}_{\mathrm{D}} \subset \mathbf{\Omega}_{\mathrm{S}}$ denote the portions of the solid domain that are fixed, located at the wedge apex and near the chine. A clamped support is imposed on these boundaries such which is mathematically given by

$$w_x(\boldsymbol{x},t) = 0, \qquad w_y(\boldsymbol{x},t) = 0, \qquad \forall \, \boldsymbol{x} \in \mathbf{\Gamma}_{\mathrm{D}}, \; t > 0. \tag{21}$$

Hence, the displacement field and any corresponding test function belonging to the admissible space can be expressed mathematically as

$$\mathcal{V}_0 = \left\{ \boldsymbol{v} \in [\mathcal{H}^1(\mathbf{\Omega}_{\mathrm{S}})]^2 \;\middle|\; \boldsymbol{v} = \mathbf{0} \text{ on } \mathbf{\Gamma}_{\mathrm{D}} \right\}. \tag{22}$$

Here, $\mathcal{V}_0$ denotes the function space containing all admissible displacement fields that satisfy the boundary conditions, $\boldsymbol{v}$ is a generic vector field belonging to this space. $\mathcal{H}^1$ represents the Sobolev space of square-integrable functions with square-integrable first derivatives defined over the domain $\mathbf{\Omega}_{\mathrm{S}}$. It should be noted that, in a two-dimensional modelling of the solid domain, the displacement field has no independent rotational degree of freedom. Therefore, setting $\boldsymbol{w} = 0$ effectively constrains both translational and rotational displacements at $\mathbf{\Gamma}_{\mathrm{D}}$, representing a clamped boundary condition. Considering this, all Dirichlet boundary conditions applied at the wedge apex and chine are enforced strongly. Yet natural traction conditions are applied on $\mathbf{\Omega}_{\mathrm{S}} \setminus (\mathbf{\Gamma}_{\mathrm{FSI}} \cup \mathbf{\Gamma}_{\mathrm{D}})$. Meanwhile, the kinematic and dynamic coupling conditions are imposed on the fluid–structure interface ($\mathbf{\Gamma}_{\mathrm{FSI}}$), as mathematically formulated in Eq. 20.

3. Numerical modelling

The numerical modelling is carried out using an open-source code named `solids4Foam` (Tuković et al., 2018), which is a package library that can be installed as an extension to the OpenFOAM-extend suite (e.g., `foam-extend-4.0`, (OpenFOAM Wiki contributors, 2016)). The code requires two computational domains, namely `fluid` and `solid`, that are coupled. The computational domains and boundaries are generated using a mesh tool, namely `blockMesh`. The problem is two-dimensional; however, a third dimension without grading is defined to enable the problem to be solved using the code.

Each block in `blockMesh` is considered to be a hexahedron. The mesh resolution in each direction of every single block is defined as

$$\Delta x = \frac{L_x}{N_x}, \quad \Delta y = \frac{L_y}{N_y}, \quad \Delta z = \frac{L_z}{N_z} \tag{23}$$

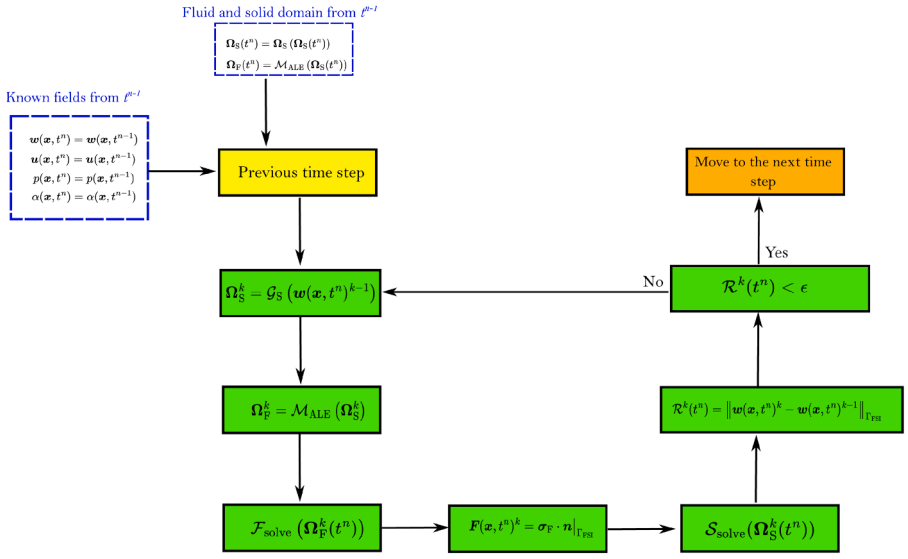

Fig. 3. Algorithm illustrating the computational approach used to solve the present FFSI problem.

where L_x , L_y , and L_z are the physical lengths of the block in each coordinate direction. N_x , N_y , and N_z are the number of cells along those directions. As said before N_z is set to be 1. The number of cells, N_x and N_y in $\mathbf{\Omega}_S$ and in the adjacent regions of $\mathbf{\Omega}_F$ on both sides of $\mathbf{\Omega}_{FSI}$, are set to be equal to ensure mesh conformity at the fluid–solid interface.

The fluid and solid dynamic problems were discretised using the Finite Volume Method (FVM) (Spalding, 1972). A first-order implicit Euler scheme was employed for the discretisation of temporal derivatives in the fluid domain ($\mathbf{\Omega}_F$). Spatial gradients and interpolations were approximated using the standard central differencing scheme (`Gauss linear`). The divergence terms in the momentum equation were discretised using a blended upwind scheme (`limitedLinearV` with a limiter coefficient of 1), which establishes a balanced compromise between the numerical stability and the solution accuracy. The volume fraction transport equation was discretised using a compressive interface-capturing scheme in combination with the `vanLeer01` limiter for convective fluxes. Laplacian terms were discretised using a corrected scheme, which can account for mesh non-orthogonality. And, meanwhile, surface-normal gradient schemes were set to `corrected` to ensure consistent estimation of the interface curvature.

The pressure field, $p(\boldsymbol{x},t)$, in $\mathbf{\Omega}_F$ is solved using the Preconditioned Conjugate Gradient (PCG) method, along with a Diagonal Incomplete Cholesky (DIC) preconditioner. In addition, the velocity field, $\boldsymbol{u}(\boldsymbol{x},t)$, was solved using the BiCGStab solver available in the code, together with the DILU preconditioning method (van der Vorst, 1992).

The mesh motion field was numerically computed over time by applying a Geometric Agglomerated Multigrid (GAMG) algorithm, which simultaneously employs Gauss–Seidel smoothing and an appropriate agglomeration control strategy.

The velocity and pressure fields are coupled and solved using the PISO (Pressure Implicit with Splitting of Operators) algorithm. One outer corrector, four pressure correctors, and a Volume of Fluid (VoF) correction were applied per time step. Furthermore, two sub-cycles were employed for the phase fraction transport equation. In this paper, the simulation of the fluid motion is denoted with $\mathcal{F}_{solve}$.

To solve the displacement field, $\boldsymbol{w}(\boldsymbol{x},t)$, in the solid domain $\mathbf{\Omega}_S$, both first-order and second-order temporal derivatives were discretised using an implicit first-order Euler scheme. An extended least-squares method was employed to reconstruct the spatial gradients of $\boldsymbol{w}(\boldsymbol{x},t)$. The divergence and Laplacian terms of $\boldsymbol{w}(\boldsymbol{x},t)$ were discretised using a second-order central differencing scheme with non-orthogonal correction. In addition, a custom block-coupled Laplacian operator (`fvmBlockLaplacian`) provided by OpenFOAM was applied.

The resulting linear system of equations for $\boldsymbol{w}(\boldsymbol{x},t)$ and its gradients $\nabla\boldsymbol{w}(\boldsymbol{x},t)$ was numerically solved using either a Preconditioned Conjugate Gradient (PCG) method with a Fast Diagonal Incomplete Cholesky (FDIC) preconditioner for non-block-coupled matrices, or a direct solver, specifically `EigenSparseLU` for block-coupled matrices.

An under-relaxation scheme is employed to prevent sudden instabilities within each iteration per time step, as given by

$$\boldsymbol{w}^{(k+1)} = (1-\omega)\boldsymbol{w}^{(k)} + \omega\boldsymbol{w}^{\text{new}}, \tag{24}$$

where $\omega \in [0,1]$ is the under-relaxation coefficient, which is set to 0.9 in the present simulations. The simulation of the fluid motion is shown with $\mathcal{S}_{solve}$.

At each time step ($t^n \rightarrow t^{n+1}$), the coupled fluid–solid motion problem is solved using a partitioned iterative algorithm (Tuković et al., 2018). In the first stage, the displacement field, velocity field, pressure field, and both the fluid and solid meshes are initialised. If it is the first time step, the fields are set to their initial values; otherwise, the solution data from the previous time step (t^{n-1}) is transferred. Accordingly,

$$\boldsymbol{w}(\boldsymbol{x},t^n) = \boldsymbol{w}(\boldsymbol{x},t^{n-1}) \qquad \forall\,\boldsymbol{x} \in \mathbf{\Omega}_S \tag{25}$$

$$\mathbf{\Omega}_S(t^n) = \mathbf{\Omega}_S\big(\mathbf{\Omega}_S(t^n)\big), \quad \mathbf{\Omega}_F(t^n) = \mathcal{M}_{ALE}\big(\mathbf{\Omega}_S(t^n)\big) \tag{26}$$

$$\boldsymbol{u}(\boldsymbol{x},t^n) = \boldsymbol{u}(\boldsymbol{x},t^{n-1}), \quad p(\boldsymbol{x},t^n) = p(\boldsymbol{x},t^{n-1}), \quad \alpha(\boldsymbol{x},t^n) = \alpha(\boldsymbol{x},t^{n-1}) \qquad \forall\,\boldsymbol{x} \in \mathbf{\Omega}_F \tag{27}$$

Then, an iterative approach is started. If it is the first iteration ($k = 1$), the solid and fluid domains are just set to be equal to those that were initialised. But if $k \neq 1$, the solid geometry ($\boldsymbol{w}(\boldsymbol{x},t)^{(k+1)}$) needs to be updated based on the solution of the previous iteration. As such, the solid geometry is first updated based on the displacement of the solid domain, as

$$\mathbf{\Omega}_S^k = \mathcal{G}_S\big(\boldsymbol{w}(\boldsymbol{x},t^n)^{k-1}\big). \tag{28}$$

Then, based on the displacement of the solid domain, the fluid domain mesh is updated as

$$\mathbf{\Omega}_F^k = \mathcal{M}_{ALE}\big(\mathbf{\Omega}_S^k\big). \tag{29}$$

Then, the fluid problem is solved using the numerical method explained earlier:

$$\boldsymbol{u}(\boldsymbol{x},t^n)^k, \quad p(\boldsymbol{x},t^n)^k, \quad \alpha(\boldsymbol{x},t^n)^k = \mathcal{F}_{solve}\big(\mathbf{\Omega}_F^k(t^n)\big).$$

Then, by integrating the pressure and shear stresses along $\mathbf{\Gamma}_{FSI}$, the traction force is obtained as

$$\boldsymbol{F}(\boldsymbol{x},t^n)^k = \boldsymbol{\sigma}_F \cdot \boldsymbol{n}\Big|_{\Gamma_{FSI}}. \tag{30}$$

The displacement field is solved using the numerical method described earlier. Hence, the structural response is updated based on the applied fluid traction forces at the fluid–solid interface:

$$\boldsymbol{w}(\boldsymbol{x},t^n)^k = \mathcal{S}_{\text{solve}}\left(\boldsymbol{F}(\boldsymbol{x},t^n)^k\right). \tag{31}$$

The residual of the displacement ($\mathcal{R}^k(t^n)$) on $\boldsymbol{\Gamma}_{\text{FSI}}$ is calculated as

$$\mathcal{R}^k(t^n) = \left\|\boldsymbol{w}(\boldsymbol{x},t^n)^k - \boldsymbol{w}(\boldsymbol{x},t^n)^{k-1}\right\|_{\Gamma_{\text{FSI}}}. \tag{32}$$

Eq. (32) serves as the convergence criterion at time step t^n. If $\mathcal{R}^k(t^n) < \varepsilon$, the iteration is terminated, and the simulation data is transferred to the next time step t^{n+1} as the initialised condition, as previously described. Otherwise, the iteration proceeds until convergence is achieved. To perform the FFSI simulations, an Aitken relaxation coefficient, ω_{A}, is applied to prevent divergence during the early iterations as follows

$$\boldsymbol{w}^k(\boldsymbol{x},t^n) = \boldsymbol{w}^{k-1}(\boldsymbol{x},t^n) + \omega_{\text{A}}\left(\boldsymbol{w}^k_{\text{raw}}(\boldsymbol{x},t^n) - \boldsymbol{w}^{k-1}(\boldsymbol{x},t^n)\right). \tag{33}$$

In Eq. (33), $\boldsymbol{w}^k_{\text{raw}}(\boldsymbol{x},t^n)$ is the direct output of the solid solver at iteration k, and $\boldsymbol{w}^k(\boldsymbol{x},t^n)$ is the relaxed displacement obtained after applying the Aitken relaxation coefficient ω_{A} (Aitken, 1926). The algorithm used to numerically solve the problem is shown in Fig. 3.

Simulations are set to start at time $t = 0$, and are run until $t = t_e$, which depends on the impact velocity (u). The FFSI is locked until $t =$ 0.002s, as a sudden noise in vibration response may happen. Yet, after this time, the FFSI modelling is set to be on, and the elastic wall is seen not to show any sudden response.

The simulations were carried out following a series of mesh sensitivity studies to determine a suitable number of cells, particularly in the blocks adjacent to the elastic walls and the free surface. The details of this analysis are presented in Appendix A. The time step was also selected based on a time step sensitivity analysis. However, the time step is dynamically controlled during the simulations, based on the Courant number (Co_{cell}), given by

$$\text{Co}_{\text{cell}} = \frac{\Delta t}{V_{\text{cell}}}\sum_f \left|\boldsymbol{u}_f \cdot \boldsymbol{S}_f\right|, \tag{34}$$

where f represents the face of a cell, $\boldsymbol{u}_f$ is the velocity vector at the cell face, $\boldsymbol{S}_f$ is the outward-pointing face area vector, and V_f is the volume of the corresponding control volume. The maximum Courant number (Co_{max}) is computed in both the fluid and solid domains, i.e., $\boldsymbol{\Omega}_{\text{F}}$ and $\boldsymbol{\Omega}_{\text{S}}$, and is used to determine the appropriate time step. A sensitivity analysis was conducted to assess the influence of Co_{max} on the simulation results, and the maximum Courant number was set to 0.25.

The simulations are not computationally expensive, as they physically model a two-dimensional water entry process. Accordingly, they were run on a single node, with each run requiring approximately 36 to 48 hours. For very stiff structures with a large Young's modulus (e.g., on the order of $\approx 200 \times 10^9$ GPa) and a low impact speed, simulations covering similar penetration depths tend to run more slowly than those with higher impact speeds. Conversely, for structures with low stiffness (e.g., on the order of $\approx 20 \times 10^9$ GPa), simulations at lower impact speeds were observed to be faster.

To provide a reference for understanding the influence of hydroelastic response on the fluid dynamics, rigid-body simulations were also conducted. In these cases, only the fluid solver, $\mathcal{F}_{\text{solve}}$, is applied in the fluid domain $\boldsymbol{\Omega}_{\text{F}}$, with mesh velocity $\boldsymbol{u}_{\text{m}} = 0$ for all cells at $t > 0$. The remaining components of the FFSI algorithm, as previously described, are omitted, and the structural solver, $\mathcal{S}_{\text{solve}}$, is not invoked in the solid domain $\boldsymbol{\Omega}_{\text{S}}$. The rigid body simulations are notably faster and can typically be completed in under 12 hours on a single node.

All simulations were carried out by setting the density of water and air to $\rho_{\text{water}} = 1000\,\text{Kg/m}^3$ and $\rho_{\text{air}} = 1\,\text{Kg/m}^3$, respectively. The dynamic viscosities of water and air were computed using the relation

$$\mu = \rho \cdot \eta, \tag{35}$$

where η is kinematic viscosity. The kinematic viscosity of water, η_{water}, is set to 1×10^{-6} m^2/s and kinematic viscosity of air η_{air} is set to be 1.8×10^{-5} m^2/s. The surface tension coefficient is set to that of the air–water interface at room temperature, with a value of $\gamma = 0.072$ N/m. All the dimensions of the domain are also set based on b as explained in Section 2. To dimensionalise the fluid and solid domains, a reference half-beam of $b = 0.5$ m is used, giving a total beam of $2b = 1$ m. This beam is comparable to the bow breadth of a high-speed planing hull with an overall length between 4 and 6 m. Nevertheless, all analyses in the present study are conducted using non-dimensionalised data.

Simulations of the present model are compared against experimental measurements (Appendices B, D and E) and previous numerical and analytical Wagner-based models (Appendices C and E) to assess the extent to which the predictions agree with, or depart from, earlier experimental, analytical and numerical studies. The comparison covers the displacement of flexible panels subjected to slamming loads (Appendices B and D), the temporal evolution of strain in the flexible panel (Appendix C) and the maximum pressure and pressure distribution along the walls of rigid wedges with different deadrise angles (Appendix E). The flexible panel validation cases are divided into two categories: panels with simply supported ends, which the present CFD–CSD model cannot ideally represent (Appendices B and C), and a panel with fixed (clamped) ends, which the model can effectively simulate (Appendix D). This comparison is conducted on purpose. It first examines how the predictions of the present CFD-CSD model aligns with experimental and numerical results for simply supported panels subjected to slamming loads, where agreements between predictions of the model and experimental/numerical results may only be achieved by assigning a lower effective elastic modulus (Appendices B and C). It then evaluates the level of accuracy of the model in predicting the dynamic response of a clamped panel under slamming load, which is the boundary condition the present framework is designed to capture reliably (Appendix D).

It is observed that the predictions of the present CFD–CSD model for the maximum panel deflection, as well as the temporal evolution of strain along the lower surface of an elastic panel with simply supported edges, are significantly under-predicted relative to both the experiments and the Wagner-based model (Appendix B and Appendix D). This outcome is not surprising, as the present CFD–CSD framework can only model solid bodies with clamped boundary conditions. The stiffness of a beam with two clamped ends is four times greater than that of a beam with two simple supports. Consequently, comparable results to both experiments and Wagner-based simulations of simply supported panels can only be achieved by prescribing a lower effective elastic modulus within the CFD–CSD model. This can be regarded as a limitation of the present CFD-CSD model. That is, it cannot reliably reproduce the dynamic response of simply supported panels subjected to slamming when the real elastic modulus is used, and a reduced effective modulus must be assigned to obtain credible results.

In contrast, the predictions of the present CFD–CSD model show very close agreement with another experimental campaign in which the boundary conditions of the flexible panel mathematically resemble clamped supports. This comparison is provided in Appendix D, where the accuray level of the CFD–CSD results are evaluated against the experimental measurements of Gilbert et al. (2023). This confirms that, although the present model cannot effectively reproduce the dynamic response of flexible panels with simple supports, it can accurately predict the response of panels with clamped ends.

Finally, the model is shown to reproduce the pressure distribution on the wedge surface with good accuracy (Appendix E). The maximum pressures for wedges with different deadrise angles are well captured when compared with experimental data, and the predictions are noticeably more accurate than those of previous Wagner-based analytical models. Technical discussions and details of the validation cases are provided in Appendices B–E.

Table 1
Test matrix with geometric and material parameters (effects of asymmetric flow pattern).

Case	β (°)	ψ (°)	β_1 (°)	β_2 (°)	u (m/s)	E (GPa)
SF-0-15	15	0	15	15	1-2-3-4-5	25 and 210
SF-0-25	25	0	25	25	1-2-3-4-5	25 and 210
SF-0-35	35	0	35	35	1-2-3-4-5	25 and 210
AF-5-20	20	5	15	25	1-2-3-4-5	25 and 210
AF-5-30	30	5	25	35	1-2-3-4-5	25 and 210

Table 2
Test matrix for AF and AR configurations with tested speeds and material stiffness (effects of flexibility).

Case	β (°)	ψ (°)	β_1 (°)	β_2 (°)	u (m/s)	E (GPa)
AF-5-20	20	5	15	25	1-2-3-4-5	10-25-50-70-210
AF-5-30	30	5	25	35	1-2-3-4-5	10-25-50-70-210
AR-5-20	20	5	15	25	1-2-3-4-5	N/A
AR-5-30	30	5	25	35	1-2-3-4-5	N/A

4. Test cases and data analysis

4.1. Tested cases

The cases studied in the present research are selected with the aim of addressing the objectives of the paper. Hence, simulations are conducted for both rigid and elastic bodies, encompassing symmetric and asymmetric settings, using the modelling framework introduced in Section 3. Various material properties are defined for the elastic bodies, permitting the investigation of how structural flexibility can influence both fluid and solid motions during the water entry process, particularly under asymmetric conditions.

Three different sets of simulations are run. In these simulations, the cases are coded as `XY-N-M`, where `X` denotes the configuration type, which is either `S` for symmetric or `A` for asymmetric. The second character, `Y`, indicates whether the simulation involves a flexible body (`F`) or a rigid body (`R`). The value `N` represents the heel angle ψ in degrees, which is 0 for symmetric cases. Finally, `M` indicates the deadrise angle β, also given in degrees.

The deadrise angle on the port side of the wedge section, β_1 ($x \in \mathbf{\Gamma}_{\mathrm{FSI}} < 0$), and on the starboard side, β_2 ($x \in \mathbf{\Gamma}_{\mathrm{FSI}} > 0$), are given by

$$\beta_1 = \beta - \psi, \quad \text{and} \quad \beta_2 = \beta + \psi. \tag{36}$$

The first set of simulations is conducted to study the effect of asymmetric fluid motion around the sections on the hydroelastic response of a wedge section entering water, with the details outlined in Table 1. Two asymmetric wedge sections with deadrise angles of $\beta = 20°$ and $\beta = 30°$, and a heel angle of $\psi = 5°$, are modelled. Additionally, three symmetric wedges with $\beta = 15°$, $\beta = 25°$, and $\beta = 35°$ are simulated, for which $\beta_1 = \beta_2$. These values either match β_1 or β_2 of the asymmetric wedge sections, providing a useful benchmark for comparing symmetric and asymmetric cases. All simulations are performed using similar impact speeds and elastic moduli. Two values of Young's modulus are considered: 210 GPa, which corresponds approximately to that of steel, and 25 GPa, which is representative of glass.

The second group of simulations, outlined in Table 2, is conducted to study the effects of elasticity on the hydroelastic responses of asymmetric wedges. Both rigid and flexible cases are considered, with two different deadrise angles, $\beta = 20°$ and $\beta = 30°$, and a heel angle of $\psi = 5°$. For the flexible cases, a wider range of Young's moduli is explored to capture the influence of structural stiffness on the fluid–structure interaction during the impact.

The third group of simulations is conducted to investigate the effects of heel angle on the dynamic response of the elastic wedge and the surrounding fluid motion during water entry. Simulations are performed for two deadrise angles, $\beta = 20°$ and $\beta = 30°$, each with heel angles of $\psi = 5°$ and $\psi = 10°$. Additionally, symmetric configurations with $\psi = 0°$ are included for reference. Both rigid and flexible cases are simulated. For the flexible configurations, only two representative Young's moduli are considered: $E = 210$ GPa and $E = 25$ GPa. The details of these cases are summarised in Table 3.

Table 3
Extended test matrix with geometry, speeds, and material stiffness values (effects of heel angle).

Case	β (°)	ψ (°)	β_1 (°)	β_2 (°)	u m/s	E (GPa)
SF-0-20	20	0	20	20	1-2-3-4-5	25 and 210
SF-0-30	30	0	30	30	1-2-3-4-5	25 and 210
AF-5-20	20	5	15	25	1-2-3-4-5	25 and 210
AF-10-20	20	10	10	30	1-2-3-4-5	25 and 210
AF-5-30	30	5	25	35	1-2-3-4-5	25 and 210
AF-10-30	30	10	20	40	1-2-3-4-5	25 and 210
SR-0-20	20	0	20	20	1-2-3-4-5	N/A
SR-0-30	30	0	30	30	1-2-3-4-5	N/A
AR-5-20	20	5	15	25	1-2-3-4-5	N/A
AR-10-20	20	10	10	30	1-2-3-4-5	N/A
AR-5-30	30	5	25	35	1-2-3-4-5	N/A
AR-10-30	30	10	20	40	1-2-3-4-5	N/A
AR-5-20	30	5	25	35	1-2-3-4-5	N/A

4.2. Data sampling

During the simulations, the full stress and strain tensors are stored, and the equivalent stress and strain are also computed. Although the problem is two-dimensional, with N_z set to 1 for all blocks in $\mathbf{\Omega}_{\mathrm{F}}$ and $\mathbf{\Omega}_{\mathrm{S}}$, the solver internally employs three-dimensional stress and strain formulations. This does not affect the results, as the out-of-plane components vanish; specifically, $\varepsilon_{xz} = \varepsilon_{zx} = \varepsilon_{yz} = \varepsilon_{zy} = \varepsilon_{zz} = 0$, and likewise $\sigma_{xz} = \sigma_{zx} = \sigma_{yz} = \sigma_{zy} = \sigma_{zz} = 0$. As such, equivalent stress is calculated as per

$$\sigma_{\mathrm{eq}} = \sqrt{\frac{1}{2}\left[(\sigma_{xx} - \sigma_{yy})^2 + (\sigma_{yy} - \sigma_{zz})^2 + (\sigma_{zz} - \sigma_{xx})^2 + 6(\tau_{xy}^2 + \tau_{yz}^2 + \tau_{zx}^2)\right]}, \tag{37}$$

$$\epsilon_{\mathrm{eq}} = \sqrt{\frac{1}{2}\left[(\varepsilon_{xx} - \varepsilon_{yy})^2 + (\varepsilon_{yy} - \varepsilon_{zz})^2 + (\varepsilon_{zz} - \varepsilon_{xx})^2 + \frac{3}{2}\left(\gamma_{xy}^2 + \gamma_{yz}^2 + \gamma_{zx}^2\right)\right]}, \tag{38}$$

where

$$\gamma_{ij} = 2\varepsilon_{ij}. \tag{39}$$

The data is analysed using two different sampling approaches, both of which rely on interpolation. The first group of sampling operations is conducted using a 1D approach, either in the fluid domain $\mathbf{\Omega}_{\mathrm{F}}$ or the solid domain $\mathbf{\Omega}_{\mathrm{S}}$, according to

$$\phi(\boldsymbol{x}_i) = \sum_{C \in \mathcal{N}} w_C(\boldsymbol{x}_i) \qquad \phi_C \in \{\boldsymbol{u}, p, \alpha\} \qquad \forall \boldsymbol{x} \subset \mathbf{\Omega}_{\mathrm{F}}, \qquad \text{and}$$
$$\phi_C \in \{\boldsymbol{w}, \sigma_{\mathrm{eq}}, \epsilon_{\mathrm{eq}}\} \qquad \forall \boldsymbol{x} \subset \mathbf{\Omega}_{\mathrm{S}}. \tag{40}$$

where ϕ_C denotes the value of the field ϕ at the centre of a neighbouring cell C, and $\phi(\boldsymbol{x}_i)$ is the interpolated value at the sample point $\boldsymbol{x}_i$. The interpolation weights $w_C(\boldsymbol{x}_i)$ vary locally and satisfy the condition

$$\sum_{C \in \mathcal{N}} w_C = 1. \tag{41}$$

The second group of sampling is done using a 2D approach, and data is found on a 2D plane $S \subset \mathbf{\Omega}_{\mathrm{F}}$ as

$$\phi(\boldsymbol{p}) = \sum_{C \in \mathcal{N}(\boldsymbol{p})} w_C(\boldsymbol{p})\, \phi_C \qquad \forall \boldsymbol{p} \in S \subset \mathbf{\Omega}_{\mathrm{F}}, \tag{42}$$

where $\boldsymbol{p}$ is a point on the interpolated plane (i.e, the sampling surface), and again w_C are the interpolated weights that satisfy Eq. 41.

4.3. Example of results

Before presenting the results and performing further analysis, a representative simulation is illustrated in Fig. 4. The results correspond to the case AF-5-20, simulated with an impact speed of $u = 4$ m/s and a Young's modulus of $E = 25$ GPa. Time histories are shown for the hydrodynamic pressure at two points located at the mid-span of the right (heeled-up, dashed red curve, $x = +b/2$) and left (heeled-down, solid red curve, $x = -b/2$) sides. In addition, the deflections at these two points, as well as the equivalent stress and strain, are presented in panels (a)–(d), respectively. All data are obtained using the one-dimensional sampling approach. The equivalent stress and strain are sampled at cells located on the left/right boundaries of the solid domain $\mathbf{\Omega}_S$, and the pressure is sampled at neighbouring cells in the fluid domain $\mathbf{\Omega}_F$.

The hydrodynamic pressure (p) shown in Fig. 4, and in all subsequent figures throughout this article, is normalised as

$$\tilde{p} = \frac{p}{\rho_{\text{water}} u^2}, \tag{43}$$

which is also known as the pressure coefficient and is commonly denoted as C_p in the literature. The deflection of any point along the wall of the wedge at every point is found as

$$\xi(x) = w_x(x)\sin\beta_1 + w_y(x)\cos\beta_1 \quad \forall x < 0 \qquad \text{and} \tag{44}$$

$$\xi(x) = -w_x(x)\sin\beta_2 + w_y(x)\cos\beta_2 \quad \forall x > 0. \tag{45}$$

It is worth noting that the displacement component w_x on the left side of the wedge, the heeled-down face ($x < 0$), is expected to be positive, while on the right side, the heeled-up face ($x \in \mathbf{\Gamma}_{\text{FSI}} > 0$), is expected to be negative during the early stage of impact, before the onset of free vibration. Deflection is normalised using the panel thickness, h.

As seen in Fig. 4a, the pressure at the midpoint is initially zero and then rises sharply. This sudden increase occurs when the spray root reaches the point. On the heeled-down side ($x < 0$), the midpoint is wetted earlier than on the heeled-up side due to the asymmetry in geometry. The peak pressure on this side reaches approximately $\tilde{p} \approx 10$, which is significantly higher than that on the heeled-up side ($\tilde{p} \approx 5.8$). After the midpoints on both sides are wetted for the first time, the pressure drops rapidly. However, this decline occurs over a very short duration ($\Delta t u/b < 0.1$, where Δt denotes the time period over which the pressure declines for the first time). A secondary peak then emerges, which is lower than the initial one, reaching $\tilde{p} \approx 6.4$ on the heeled-down side and $\tilde{p} \approx 4.3$ on the heeled-up side. This second peak is attributed to the dynamic response of the elastic wall of the wedge on both sides. Following this, the pressure at the midpoint on both sides oscillates with a nearly constant frequency, while the amplitude decays exponentially over time. Interestingly, the pressure on the left side of the wedge, corresponding to the heeled-down face, can become negative during the oscillation phase. This is likely due to large negative values of the vertical velocity component ($\dot{\xi}$), which arise from the dynamic response and free vibration of the structure. On the side with a lower deadrise angle ($x < 0$), both the deflections and the rate of deflection during the free vibration phase can be significant, potentially resulting in negative pressure when $\dot{\xi} < 0$. Such an effect is not expected to occur at lower impact velocities (e.g., $u = 1$ m/s).

The time history of the deflection at the midpoints on both sides of the wedge (Fig. 4b) clearly demonstrates the dynamic response of the flexible wedge wall during water impact. The deflection at each midpoint initially rises to a maximum value, followed by a phase of free vibration. Evidently, this peak deflection occurs concurrently with the appearance of the second pressure peak in the corresponding pressure time history (Fig. 4a). Subsequently, both midpoints exhibit oscillatory motion, with the amplitude of oscillation decaying exponentially over time. The peak deflection at the midpoint of the side with the lower deadrise angle (the heeled-down side, $\xi/h \approx 0.43$) is greater than that of the side with the higher deadrise angle (the heeled-up side, $\xi/h \approx 0.24$). Since the deflection arises directly from pressure loading, and both sides possess similar rigidity (EI/h^3), it can be concluded that the larger deflection on the heeled-down side results from the higher pressure acting on that side.

The normalised equivalent stress acting on the section, calculated as

$$\tilde{\sigma}_{\text{eq}} = \frac{\sigma_{\text{eq}}}{\rho_{\text{water}} u^2}, \tag{46}$$

is observed to reach a peak value on both sides (Fig. 4c), coinciding precisely with the time at which the deflection peaks at each respective side. This indicates that the stress within the solid structure arises as a direct consequence of its dynamic response. The time history of the equivalent stress exhibits oscillations with a frequency similar to that of the deflection and pressure at the midpoint on both sides. However, unlike pressure, the stress remains non-negative.

The temporal evolution of the equivalent strain, ϵ_{eq}, closely follows that of the equivalent stress. The peak strain on the heeled-down side is notably larger, which is attributed to the higher hydrodynamic pressure and greater deflection observed on this side. The similarity in the time evolution of equivalent stress and strain is expected, given the direct constitutive relationship between the two.

The distribution of pressure (Fig. 4e) along the wall of the wedge exhibits a clear asymmetry pattern. Prior to the water reaching the chine on either side, pressure peaks occur at the spray root location. The wetted region of the wedge can be tracked by observing the movement of the location where the peak pressure emerges. On the heeled-down side, which features a lower deadrise angle, the wetted area expands more rapidly. The temporal peak pressure on both sides increases prior to flow separation (i.e., the transition to a fully wetted condition). This observation stands in contrast to the assumptions of similarity solutions, which typically posit that the pressure distribution maintains a consistent shape during the early stages of water entry.

The deflection pattern of the wedge wall displays a clear asymmetry (Fig. 4f), consistent with the pressure distribution. The panels on both sides of the wedge bend upward throughout the simulation. Initially, the maximum bending occurs between the wedge apex and the location of the spray root, up to the point where approximately half of the panel becomes wetted. Beyond this stage, the maximum deflection shifts to the midpoint of each panel ($x = -b/2$ and $x = b/2$). The temporal maximum bending amplitude is observed to decrease after flow separation. That is, it happens when the entire panel is wetted, which coincides with the sudden drop in pressure.

The stress and strain distributions along the wall of the elastic wedge exhibit similar patterns (Fig. 4g and h), consistent with the time histories observed at the midpoints on both sides (Fig. 4c and d). The maximum temporal stress and strain initially occur near the wedge apex at the onset of the water entry. A secondary peak is also observed, emerging at the locations where the maximum temporal deflection occurs. This secondary peak appears at $x = -b/2$ on the heeled-down side and $x = b/2$ on the heeled-up side after the corresponding side becomes fully wetted. Subsequently, the onset of the free vibration phase results in oscillatory behaviour in both stress and strain, which gradually decays over time.

Additional parameters useful for interpreting the fluid motion around the section are presented in Fig. 5. All of these quantities are computed using one-dimensional sampling within the fluid domain, $\mathbf{\Omega}$F. The first parameter is the half-wetted beam of the wedge wall, calculated as

$$c = \int_l \alpha dx. \tag{47}$$

c is initially zero, as the wedge wall has not yet contacted the water. As the water advances toward the wedge, c increases until $c/b = 1$, indicating that the entire wall has been wetted and flow detachment has occurred. The other parameter is the time rate of the half-wetted beam, $\dot{c}$, which measures how quickly the half-wetted beam grows with time.

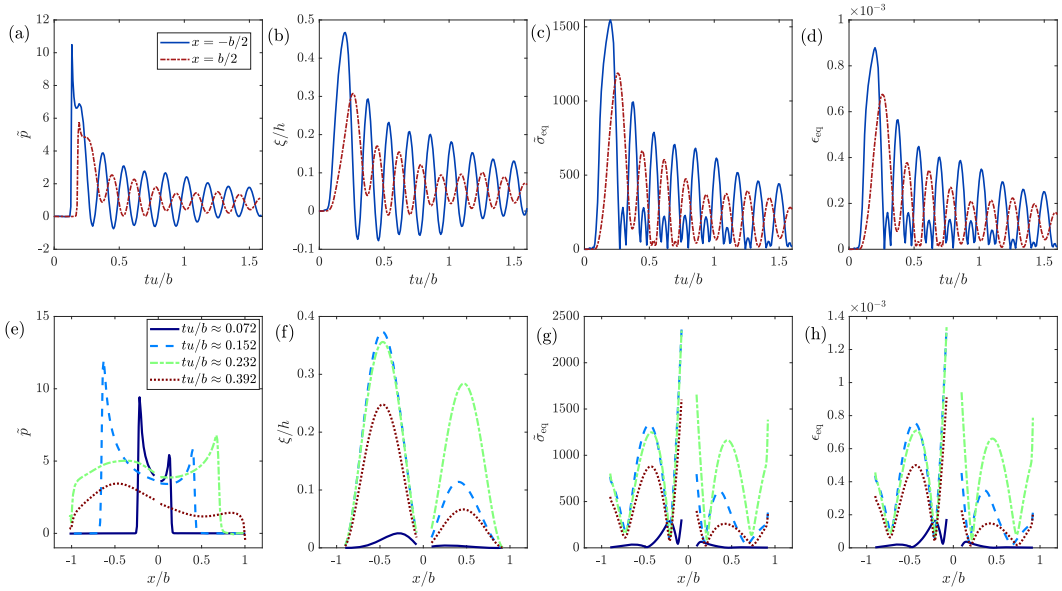

Fig. 4. Representative time histories (a–d) and spatial patterns (e–h) of the hydrostructural response of a heeled elastic wedge ($\beta_1 = 15$ and $\beta_2 = 25$) impacting the water surface at a constant velocity of $u = 4$ m/s. Shown are the temporal evolution and transverse distributions of pressure (a, e), deflection (b, f), equivalent von Mises stress (c, g), and equivalent strain (d, h). This simulation corresponds to case AF-5-20, as defined in the present study, and $E = 25$ GPa.

$\dot{c}$ is normalised by its theoretical value, $\dot{c}_t$, obtained from the Wagner boundary condition (Wagner (1932)), which is expressed as

$$\dot{c}_t = \frac{\pi}{2}\frac{u}{\tan\beta_1} \qquad x < 0 \qquad \text{and} \qquad \dot{c}_t = \frac{\pi}{2}\frac{u}{\tan\beta_2} \qquad x > 0. \tag{48}$$

Theoretically, $\dot{c}$ is expected to be 1.0 during the whole water entry process, but as seen, it may vary over time. On the heeled down side ($x < 0$ and $\beta_1 = 15$), $\dot{c}_1$ is close to 1.1, but it suddenly increases and reaches up to 1.5. On the right side ($x > 0$ and $\beta_1 = 25$), a similar pattern for time history of $\dot{c}_2$ can be seen, but intrestingly $\dot{c}_2/\dot{c}_t$ is below 1, and it show a very weak peak before flow seperation.

The other parameter presented in Fig. 5 is the average value of velocity magnitude. The velocity magnitude, defined as

$$|\boldsymbol{u}| = \sqrt{u_x^2 + u_y^2}, \tag{49}$$

and its temporal average value along the wall of the wedge on each side is calculated as

$$\langle|\boldsymbol{u}|\rangle = \frac{\int |\boldsymbol{u}|\alpha d x}{\int \alpha d x}. \tag{50}$$

The average value of the velocity magnitude along the wall on the heeled-up side of the wedge is observed to be higher. This is likely because the wedge on that side has a larger deadrise angle, allowing water to move more freely towards the chine. This indicates that the fluid momentum is reduced less on this side of the wedge, and consequently, the resulting pressure and hydrodynamic force are lower compared to the heeled-down side.

Snapshots from the simulation of the example case are also presented in Fig. 6 to provide a clearer illustration of the velocity and pressure fields around the section during the water entry process. The deflection patterns on both the heeled-down and heeled-up sides of the wedge are shown using curves that are not to scale, as the deflections are of the order of 0.1mm. The curves at each time step are coloured from light grey to black, with darker shades indicating larger deflections.

The data presented in this Figure is sampled using the two-dimensional sampling approach, and the deflection is sampled using a one-dimensional approach. At the early stage of impact ($tu/b \approx 0.072$), high-pressure contours appear on the left side of the wedge, and on both sides, a concentrated pressure zone forms near the spray root. The average velocity magnitude normalised by the impact speed u, is observed to be significantly larger near the spray root and along the free surface close to the wedge wall, whereas in the bulk of the fluid domain, it is close to u (i.e., $|\boldsymbol{u}|/u \approx 1$). The panels exhibit deflection on both sides of the wedge, with the heeled-down side showing the larger response owing to the higher pressure acting on that side. As water wets a greater length on both sides of the wedge ($tu/b \approx 0.152$), the pressure distribution extends over a larger area. As observed, broader regions of elevated pressure develop around the wedge section. At this stage of the water entry process, the velocity field becomes more developed, with high-velocity spray regions forming near the wedge walls.

Flow separation first emerges on the heeled-down side (Fig. 6c and h), leading to a noticeable pressure drop on that side. At this stage, a splash flow detaches from the chine, leaving the wedge at an angle steeper than β_1. Near the chine, the pressure approaches zero, as expected, while the velocity magnitude of the splash fluid is observed to be higher than that of the spray root formed along the wall prior to flow separation. On the opposite, heeled-up side, high pressure continues to act on the wedge wall. Eventually, at approximately $tu/b \approx 0.312$, flow detachment occurs on the heeled-up side as well, resulting in a pressure drop and the formation of splash flow similar to that observed on the other side. However, the kinematics of the splash on the two sides are expected to differ, an interesting physical problem not addressed in the present study. Notably, on the left (heeled-down) side of the wedge, the pressure is seen to increase again around the midsection of the wall compared to the previous stage (Fig. 4c), clearly indicating that the dynamic response of the wedge wall influences the pressure field around the structure. On both sides of the wedge, the deflection is markedly reduced immediately after flow detachment from the chine, as the impact pressure is released. Yet, because the panel undergoes a whipping-like dynamic response, the deflection may increase again as the penetration depth grows. This continues until the deflections fully decay. This behaviour is evident when comparing the deflection curves on the heeled side at $tu/b \approx 0.272$, corresponding to an instant shortly after flow separation, and at $tu/b \approx 0.312$, when the penetration depth has increased.

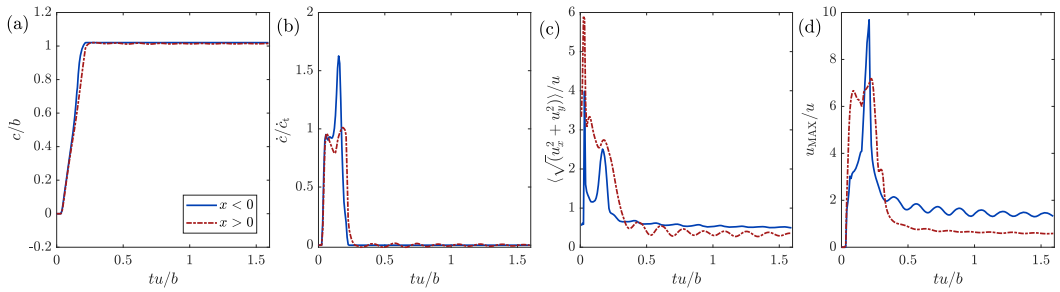

Fig. 5. Representative time histories (a–d) and spatial patterns (e–h) of the hydrostructural response of a heeled elastic wedge ($\beta_1 = 15$ and $\beta_2 = 25$) impacting the water surface at a constant velocity of $u = 4$ m/s. This simulation corresponds to case AF-5-20, as defined in the present study, and $E = 25$ GPa.

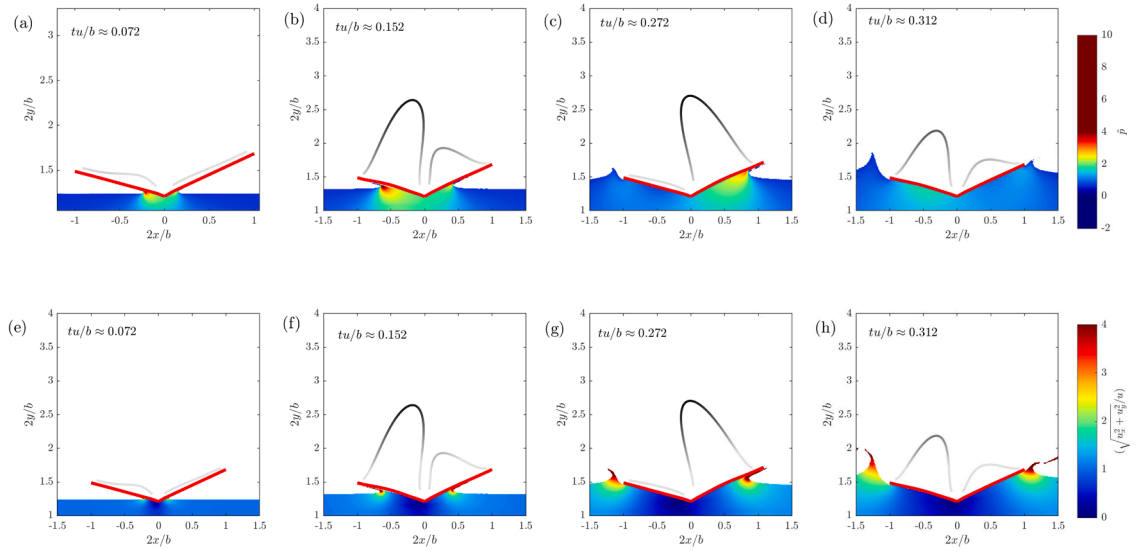

Fig. 6. Instantaneous pressure (top row, panels a–d) and velocity-magnitude, $|\boldsymbol{u}|$, (bottom row, panels e–h) fields around a heeled elastic wedge impacting the water surface at a constant speed of 4 m/s. Columns in this Figure correspond to the non-dimensional times $tu/b \approx 0.072$ (a, e), 0.152 (b, f), 0.272 (c, g), and 0.312 (d, h). Flow detachment initiates on the heeled-down face between $tu/b \approx 0.152$ and 0.272 and is complete on both faces by $tu/b \approx 0.312$. Here t is time, u is the impact speed, and b is half-beam of the wedge section. The deflection of the flexible panels on both sides of the wedge is shown using curves that are not to scale, with darker colours indicating larger deflections. Results correspond to the simulation case AF-5-20 with Young's modulus $E = 25$ GPa, as defined in the present article.

5. Results and discussions

5.1. Effects of asymmetric condition

The effects of asymmetric conditions on the hydroelastic response of the wedge are examined through analysis of the cases summarised in Table 1. To facilitate comparison between symmetric and asymmetric configurations, results from the sides of wedges with matching deadrise angles are directly compared.

Time histories of hydrodynamic pressure at the midpoint of the wedge for the asymmetric cases exhibit noticeable deviations from those of the symmetric configurations, as observed in Fig. 7a and e. This provides early but important evidence that asymmetry can influence the pressure acting on a wedge-shaped body entering water.

On the left side of an asymmetric wedge ($x = -b/2$), where $\beta_1 < \beta_2$, the peak pressure occurring at the moment the spray root intersects the midpoint is observed to be lower than that of a symmetric wedge ($\beta_1 = \beta_2$) with an equivalent deadrise angle (Fig. 7a). Similarly, the pressure fluctuations induced by the whipping response of the elastic wedge wall are also reduced in the asymmetric configuration. In contrast, on the right side, corresponding to the heeled-up side of the wedge (where $\beta_1 > \beta_2$), the peak pressure exceeds that of the symmetric case ($\beta_1 = \beta_2$), with the same deadrise angle on that side. Moreover, the pressure fluctuations on the heeled-up side of the wedge, emerging during whipping, are also greater than those observed in the symmetric case.

The effects of the asymmetric flow pattern on the dynamic response of both sides of the wedge (Figure 7b and f) are consistent with those observed in the pressure histories, which is physically reasonable given the strong coupling expected between hydrodynamic pressure and structural deflection during impact. The heeled-down side of the asymmetric flexible wedge undergoes smaller deflections as compared to the symmetric wedge with the same deadrise angle, whereas the heeled-up side undergoes larger peak deflection, followed by more pronounced oscillations during the whipping phase.

Time histories of pressure and deflection also reveal that the natural period associated with the lowest mode of panel vibration is reduced in the asymmetric condition as compared to symmetric ones with similar local deadrise angles. On the heeled-down side, the natural period of the lowest mode is 0.0203 s, whereas the corresponding value for the symmetric wedge is 0.0250 s. On the heeled-up side, the natural period is 0.0209 s, in contrast to 0.0284 s for the symmetric case. This reduction is attributed to the added mass associated with the first mode of vibration on each side of the wedge. Theoretically, the natural period is directly proportional to the square root of the added mass; hence, the observed shortening of the natural period corresponding to the lowest mode implies a reduction in added mass on both sides of the wedge due to the asymmetric flow field.

The time rate of change of the horizontal spray root velocity is found to be influenced by the asymmetric flow pattern, with distinct effects observed on each side of the flexible wedge (Fig. 7c and g). On the

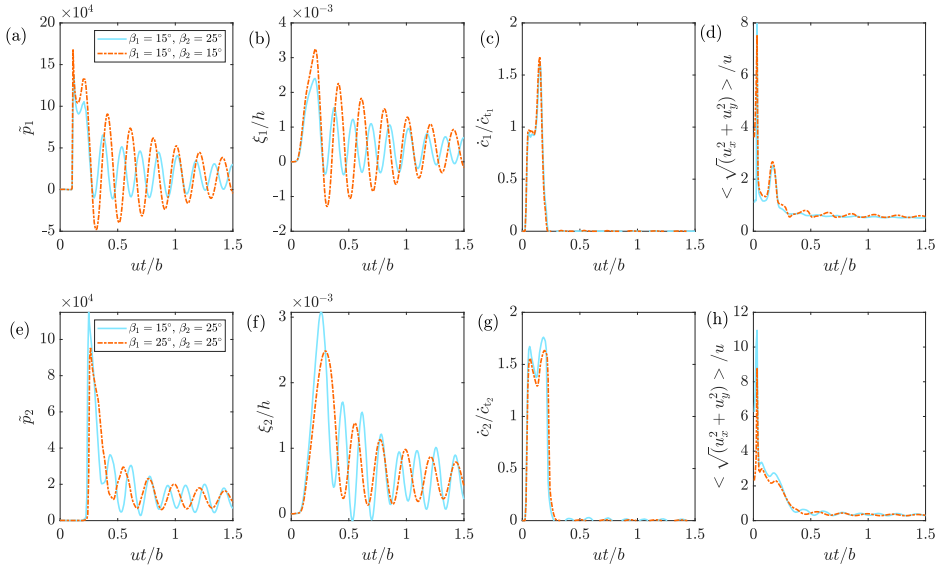

Fig. 7. Time histories of pressure (a, e) and deflection (b, f) at the midpoint of symmetric and asymmetric flexible wedges, alongside the instantaneous horizontal velocity of the spray root (c, g) and the average wall-parallel velocity along the wedge surface (d, h). The upper panels (a-d) compare the heeled-down side of an asymmetric wedge with a symmetric wedge (both with $\beta_1 = 15°$), while the lower panels (e-h) compare the heeled-up side of an asymmetric wedge with a symmetric wedge (both with $\beta_2 = 25°$).

heeled-down side, the asymmetric flow decelerates the spray root propagation, whereas on the heeled-up side, an acceleration is observed. This indicates that heel asymmetry may redistribute momentum preferentially towards the heeled-up side, where the fluid is less constrained and can more readily travel towards the chine. This asymmetric momentum transfer likely accounts for the reduced pressure on the heeled-down side during impact, compared to a symmetric wedge with the same local deadrise angle, and the increased pressure on the heeled-up side under the same comparison. Such behaviour highlights a key influence of asymmetric flow patterns on impact pressure during the water entry process, and, consequently, on the resulting dynamic response and structural deformation of the flexible wedge.

The temporally averaged velocity along the wedge surface (7d and h) similarly reflects the trends observed in the horizontal spray root velocity, providing further support for the hypothesis of greater momentum transfer towards the heeled-up side during the water entry process.

To provide a clearer picture of the effects of asymmetric flow patterns on the pressure distribution along the wall of an elastic wedge, pressure profiles at two distinct time instants, $tu/b \approx 0.112$ and $tu/b \approx 0.192$, both corresponding to the dry-chine condition, are presented in Fig. 8. At both instants, notable differences are observed between the pressure distributions of the symmetric and asymmetric cases. On the heeled-down side of the asymmetric wedge, the peak pressure, as well as the distributed pressure along the wetted surface, is consistently lower than that of the symmetric wedge with the same local deadrise angle. In particular, the contact region is reduced for the asymmetric case. This observation is consistent with the results shown in Fig. 7c, where the spray root on the heeled-down side exhibited a slight deceleration during asymmetric water entry.

Conversely, on the right side of the wedge, corresponding to the heeled-up configuration, the hydrodynamic pressure acting on the asymmetric wedge is greater than that on the symmetric wedge at both time instants. Interestingly, the contact region in the asymmetric case is again found to be reduced relative to the symmetric counterpart. This aligns with the behaviour observed in Fig. 7g, where the spray root velocity on the heeled-up side was seen to accelerate under asymmetric conditions, in comparison with the symmetric case.

A comprehensive comparison between the hydrostructural responses of symmetric and asymmetric elastic wedges is presented in Figs. 9 and 10, including all simulation cases listed in Table 1. The focus is placed on the peak values recorded at the midpoint of the wedge, which are taken as representative indicators of the overall hydrostructural response. In all Figures, subscripts 1 and 2 refer to quantities associated with the left and right sides of the wedge, respectively. For the asymmetric wedge, subscript 1 corresponds to the heeled-down side, and subscript 2 corresponds to the heeled-up side.

As seen in Figs. 9 and 10, the hydrostructural responses of both symmetric (blue markers) and asymmetric (orange markers) elastic wedges are influenced by the water entry speed, u. This dependence indicates the presence of nonlinear effects, likely arising from variations in the spray root pattern and water surface elevation around the wedge during the water entry process.

The normalised peak pressure is observed to decrease with increasing impact speed (Fig. 9a, b, e, f and Fig. 10a, b, e, f). However, this reduction becomes minimal when the local deadrise angle is 35° (see Figs. 10e and f). In contrast, the normalised peak deflection (ξ/h) increases with impact speed (Fig. 9c, d, g, h and Fig. 10c, d, g, h). This trend is theoretically anticipated, as the peak normalised deflection depends on the dimensional peak pressure (p), which increases with speed (u), rather than on the normalised peak pressure itself ($\tilde{p}$).

The normalised peak equivalent stress ($\tilde{\sigma}_{\mathrm{eq}}$) is observed to increase with impact speed on both sides of the symmetric (blue markers) and asymmetric (orange markers) wedges (Fig. 9k, l, o, p and Fig. 10k, l, o, p), with the exception of the side having a deadrise angle of 35°, for which no clear dependence on speed is evident.

The normalised peak horizontal velocity of the spray root ($\dot{c}_i/\dot{c}_{\mathrm{t}}$) as a function of impact speed exhibits distinct trends across different cases (Fig. 9i, j, m, n and Fig. 10i, j, m, n). This is particularly noteworthy, as $\dot{c}/\dot{c}_{\mathrm{t}}$ represents one of the key indicators potentially affecting the peak pressure response.

To examine the effects of asymmetric flow patterns on the hydroelastic response of a wedge entering water, the heeled-down side of the wedge (left side, shown with subscript 1) is considered. On this side, as evident from Fig. 9a, b, e, and f, the normalised peak pressure emerging

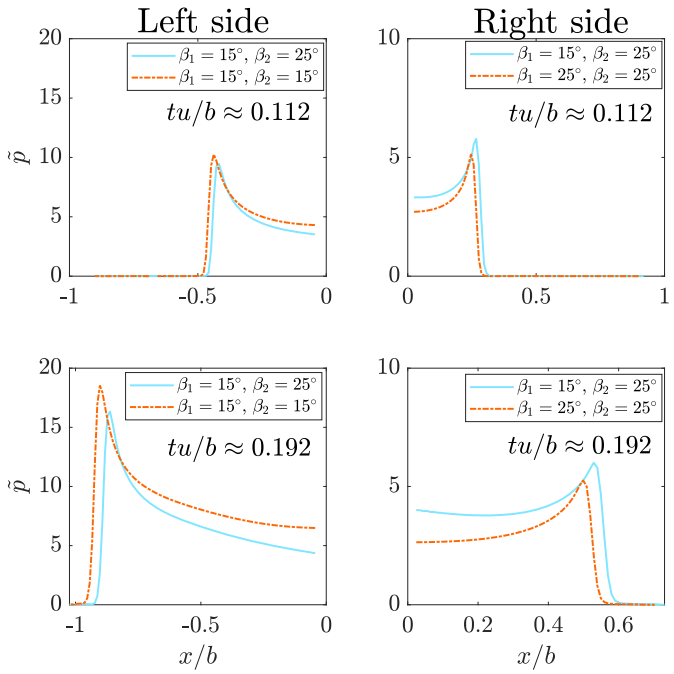

Fig. 8. Pressure distribution along the wall of flexible symmetric (dashed curves) and asymmetric wedges (solid curves) at two different time instants. The left and right panels show the pressure distribution on the left and right sides of the wedges, respectively. For the asymmetric cases, the curves correspond to the heeled-down and heeled-up sides. The results are for an impact speed of 4 m/s and an elastic modulus of 25 GPa.

on the symmetric wedge is generally higher than that on the corresponding heeled-down side of the asymmetric wedge with the same local deadrise angle (β_1). An exception is noted for the case with $\beta_1 = 15°$ and high structural stiffness (Fig. 9 b). This trend is consistent with the observed larger normalised peak deflection in the symmetric configuration compared to the asymmetric one (Figs. 9 c, d, g, and h).

On the heeled-down side of an asymmetric wedge entering water, the peak normalised horizontal velocity of the spray root ($\dot{c}_1/\dot{c}_t$) is clearly lower than that of the symmetric wedge with the same local deadrise angle (β_1). This observation lends further support to the earlier hypothesis regarding the influence of asymmetric flow on pressure and fluid momentum, as discussed in relation to the results in Fig. 7. At all tested considered water entry speeds (u), the spray root on the heeled-down side is decelerated compared to a symmetric wedge with similar β_1, which likely linked to the observed reduction in pressure relative to that of a symmetric wedge with identical local geometry.

Finally, the peak normalised equivalent stress on the heeled-down side of the asymmetric wedge ($\tilde{\sigma}_{eq}$) is consistently lower than that of the symmetric wedge with the same local deadrise angle across all impact speeds (Fig. 9k, l, o, p). This observed behaviour matches the previously discussed effects of asymmetric flow on the normalised peak pressure and normalised peak deflection.

On the heeled-up side of an asymmetric wedge (Fig. 10), the effects of asymmetric flow on the peak normalised pressure, peak normalised deflection, peak normalised horizontal velocity of the spray root ($\dot{c}_2/\dot{c}_t$), and peak normalised equivalent stress at the midpoint are observed to be opposite to those on the heeled-down side (Fig. 9). This is mostly because this side of an asymmetric wedge has a relatively large deadrise angle, and hence, the flow tends to move towards this side. For instance, the peak normalised pressure ($\tilde{p}_{2,MAX}$) on the heeled-up side of the asymmetric wedge exceeds that of the symmetric wedge with the same local deadrise angle across all impact speeds considered. This trend is similarly reflected in the corresponding increases in peak normalised deflection and peak normalised equivalent stress.

An interesting observation on the heeled-up side of the wedge pertains to the normalised horizontal velocity of the spray root ($\dot{c}_2/\dot{c}_t$) for the flexible asymmetric wedge with $\beta_2 = 35°$ for both considered Elastic modulii. While the spray root velocity on the asymmetric wedge is consistently higher than that of the symmetric counterpart, it is observed to decrease with increasing impact speed, u, a trend not seen in the symmetric case. This behaviour may be attributed to several factors, one plausible explanation being the partial dissipation of energy within the spray root region at higher impact speeds.

Focusing solely on the peak normalised pressure and the hypothesis that it is governed by the peak normalised horizontal velocity of the spray root ($\dot{c}_i/\dot{c}_t$), these two quantities are plotted against each other. To this end, the relative change in peak normalised pressure due to the presence of asymmetric conditions is introduced as

$$\tilde{\Delta}\tilde{p}_{MAX} = \frac{\tilde{p}^{asy}_{MAX} - \tilde{p}^{sy}_{MAX}}{\tilde{p}^{sy}_{MAX}}, \tag{51}$$

and is plotted against the relative change in peak normalised horizontal speed of the spray root, which is introduced as

$$\tilde{\Delta}\dot{c} = \frac{\dot{c}^{asy} - \dot{c}^{sy}}{\dot{c}^{sy}}. \tag{52}$$

In the calculation of $\tilde{\Delta}\tilde{p}_{MAX}$ and $\tilde{\Delta}\dot{c}$, the relative changes due to the asymmetric (asy) condition are evaluated with respect to the corresponding symmetric (sy) configuration having the same local deadrise angle and structural stiffness. As a result, two sets of relative changes are calculated. One corresponds to the heeled-down side and the other to the heeled-up side.

The data are plotted in the $\tilde{\Delta}\tilde{p}_{MAX}$–$\tilde{\Delta}\dot{c}$ plane. A point lying at the origin of this plane indicates that the introduction of asymmetry produces no change in either the peak normalised pressure or the peak normalised horizontal velocity of the spray root. Scatter plots of the relative change in pressure versus the relative change in horizontal spray root velocity are presented in Fig. 11, with the left and middle panels corresponding

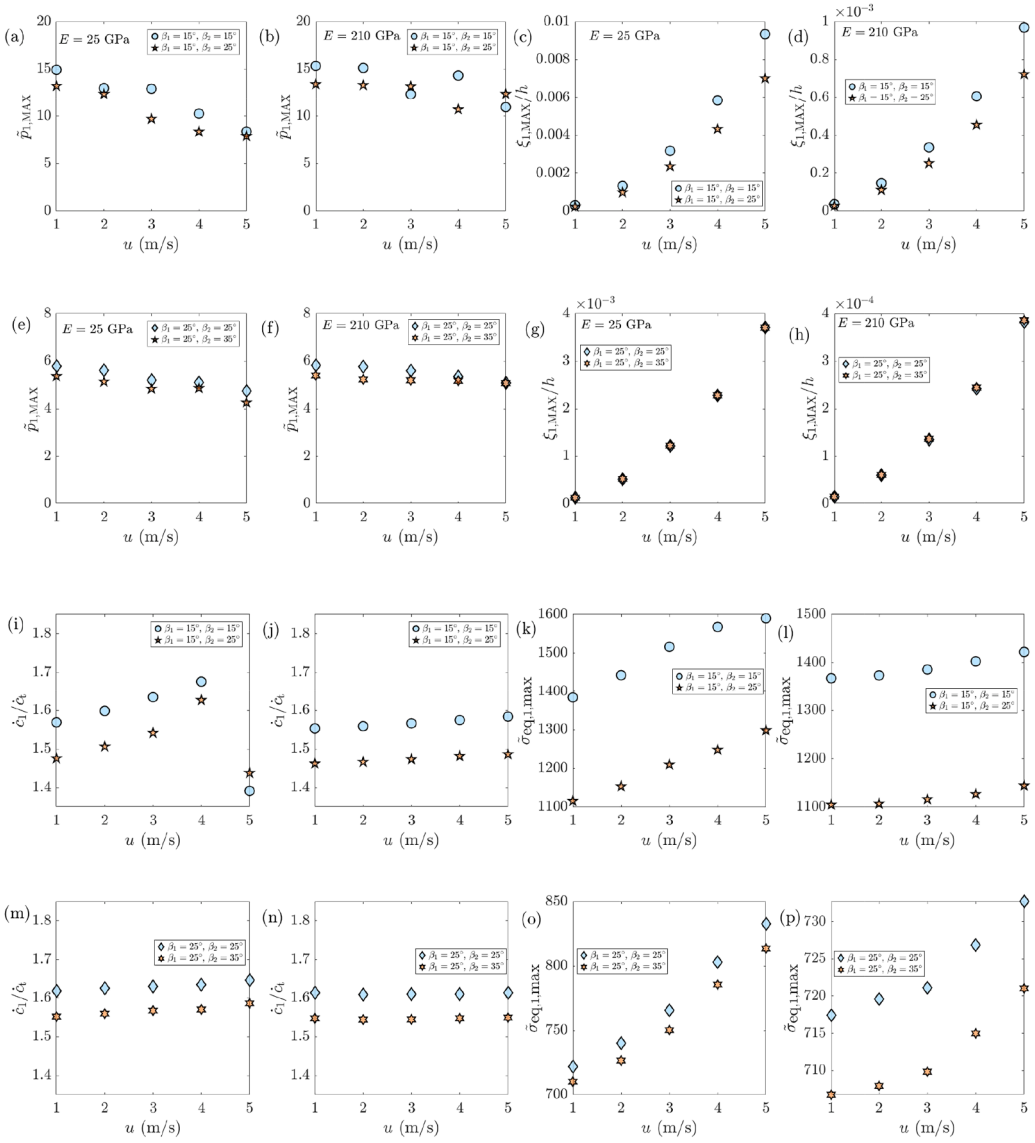

Fig. 9. Effects of asymmetric flow patterns on the maximum normalised pressure $\tilde{p}_{\mathrm{MAX}}$ (panels (a), (b), (e), (f)), normalised deflection ξ_{MAX}/h (panels (c), (d), (g), (h)), horizontal velocity of the spray root (panels (i), (j), (m), (n)), and maximum normalised equivalent stress (panels (k), (l), (o), (p)) at various water-entry velocities. All results correspond to the left-hand side of the wedge and compare the heeled-down side of an asymmetric wedge with those of a symmetric wedge possessing the same local deadrise angle β_1. The results are presented for two different elastic moduli of $E = 25$ GPa and $E = 210$ GPa.

to the heeled-down and heeled-up sides of the wedge, respectively. In this Figure, marker size is scaled according to the impact speed (u), and marker colour indicates the elastic modulus: yellow for the lower modulus ($E = 25$ GPa) and orange ($E = 210$ GPa) for the higher modulus.

As seen, most of the data points related to the heeled-up side of the wedge lie in the third quadrant of the $\tilde{\Delta}\tilde{p}_{\mathrm{MAX}} - \tilde{\Delta}\dot{c}_{\mathrm{MAX}}$ plane. This clearly indicates that both the horizontal spray root velocity and the peak pressure on the heeled-down side of the wedge are lower than those of a symmetric wedge with the same local deadrise angle. A clear proportional relationship is observed between $\tilde{\Delta}\tilde{p}_{\mathrm{MAX}}$ and $\tilde{\Delta}\dot{c}$, and a best-fit line passing through the origin is found to approximate the data asymptotically. The maximum relative reduction in peak pressure on the heeled-down side, compared to the symmetric case, is approximately 25 %, corresponding to a 12 % relative reduction in spray root velocity.

Interestingly, all data points representing the effects of asymmetric conditions on the heeled-up side lie in the first quadrant of the $\tilde{\Delta}\tilde{p}_{\mathrm{MAX}}$–$\tilde{\Delta}\dot{c}$ plane. The maximum relative increase in peak pressure on the heeled-up side reaches approximately 20 %, while the corresponding increase in the horizontal velocity of the spray root is up to 10 %. Once again, a line passing through the origin $\langle 0, 0\rangle$ is fitted to the data, suggesting a proportional relationship between these two physical quantities.

In the right panel of Fig. 11, data points representing the effects of asymmetric flow patterns on both the heeled-up and heeled-down sides of the wedge are presented, with the aim of comparing the slopes of the fitted lines corresponding to each side. Evidently, the red dashed line associated with the heeled-down side exhibits a steeper slope than the blue dashed line, which corresponds to the heeled-up side. This provides evidence that the influence of asymmetry may be more remarkable on the heeled-down side of the asymmetric elastic wedge.

5.2. *Effects of flexibility*

The results presented in Table 2 are analysed in this sub-section. Fig. 12 shows representative time histories of the normalised pressure and deflection at the midpoints of the heeled-down and heeled-up sides of the wedge, together with the normalised horizontal speed of the spray root and the temporal average velocity. The results correspond to a

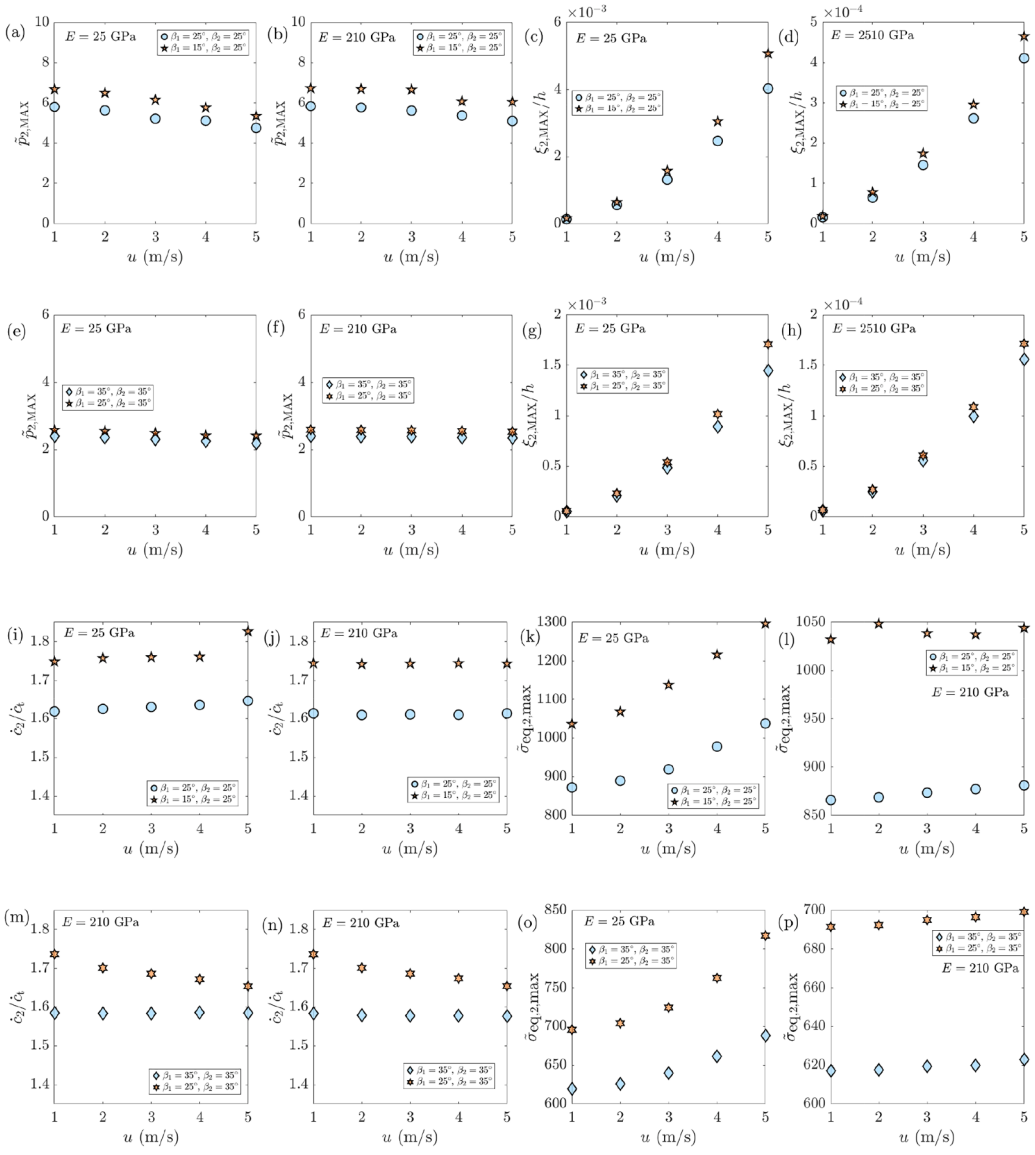

Fig. 10. As of Figrue 9, but for the right side of the wedge. That is, the results compare the heeled-up side of an asymmetric wedge with those of a symmetric wedge with the same local deadrise angle β_2.

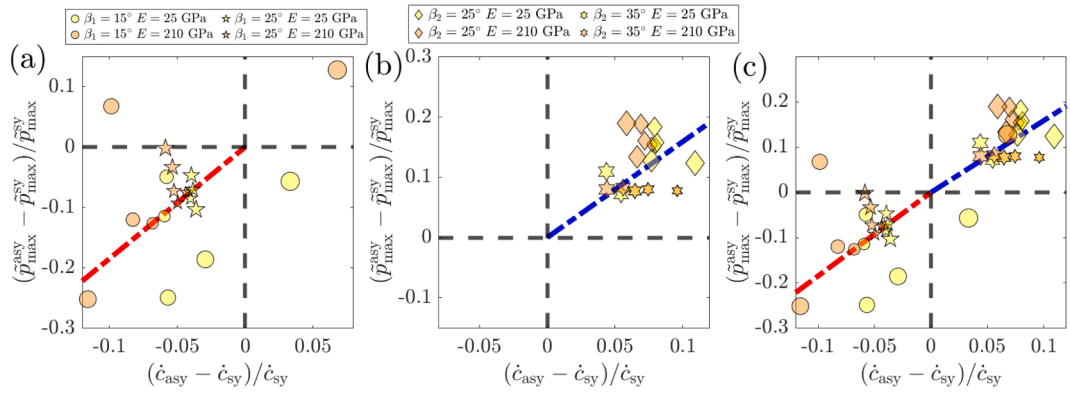

Fig. 11. Effects of asymmetric flow pattern on peak pressure and horizontal velocity of the spray root, shown in the $\tilde{\Delta}\tilde{p}_{MAX}$–$\tilde{\Delta}\dot{c}$ plane. The left panel presents data for the left (heeled-down) side of the asymmetric wedge, the middle panel corresponds to the heeled-up side, and the right panel shows data for both sides. Lines approaching the asymptotic limits are also plotted, with their slopes determined via least-squares fitting.

wedge with deadrise angles of 20°, and a heel angle of $\psi = 5°$, and are presented for three cases: a rigid wedge, a flexible wedge with $E = 50$ GPa, and a flexible wedge with $E = 20$ GPa.

The normalised pressure at the midpoint of the panel on both sides is evidently higher for the rigid body during water entry, as compared to the flexible cases. The peak pressure decreases with decreasing elastic modulus. This provides compelling evidence that structural flexibility reduces the peak impact pressure during the water entry process, and is matching with observations made by different researchers over the past decade.

The pressure acting at the midpoint on both sides of the rigid body exhibits a sharp decline immediately after the peak, followed by a secondary drop associated with flow separation from the chine. Thereafter, the normalised pressure on both sides of the wedge decreases slightly and asymptotically approaches a constant positive value. In contrast, the temporal evolution of normalised pressure for the flexible wedges displays different characteristics. Following the initial peak, a secondary peak may or may not emerge prior to flow separation. This secondary peak is observed on the heeled-down side (left side) for both elastic moduli; however, on the heeled-up side (right side), it appears only in the case with the lower elastic modulus. This secondary peak is attributed to the structural modal response and coincides with the first significant peak in panel deflection.

The time history of normalised deflection at the midpoint of both elastic wedges reveals that the peak deflection on both sides is greater for the case with the lower elastic modulus. Interestingly, the oscillations in pressure and deflection at the midpoint of the more rigid wedge (i.e., with the higher elastic modulus) occur with a shorter period. This is consistent with theoretical expectations, as the natural frequencies of a vibrating panel are proportional to the square root of the elastic modulus, i.e., $\omega_n \propto \sqrt{E}$, and consequently $T_n \propto \sqrt{E}^{-1}$. Notably, in the time histories plots of pressure and deflections of the wedge with a larger elastic modulus, the oscillatory response of both pressure and deflection exhibits irregularities on both sides. That is, the whipping response does not decay in a clearly exponential manner, suggesting the possible excitation of higher-order structural modes, such as those corresponding to the second and third natural frequencies, contributing to the overall dynamic response, which exhibits irregular behaviour.

The horizontal speed of the spray root is influenced by structural flexibility and elastic modulus, generally showing a reduction with increased flexibility. On the heeled-down side of the wedge (Fig. 12c), flexibility leads to a noticeable decrease in $\dot{c}_1$ throughout the water entry phase, up until flow separation. This clearly indicates that a portion of the fluid momentum is transferred to the solid structure; consequently, the spray cannot propagate as rapidly as it does in the rigid case. This observation likely explains the lower impact pressures experienced by the flexible wedge. Interestingly, at the onset of flow separation, the horizontal spray root speed on the heeled-down side becomes larger for the flexible cases than for the rigid case. This may be attributed to the structural response, whereby momentum is returned from the solid to the fluid, manifesting as an acceleration of the spray root.

On the heeled-up side of the wedge (Fig. 12g), a reduction in the horizontal speed of the spray root is observed during the water entry phase. This reduction is likely a contributing factor to the lower impact pressures recorded on this side. However, unlike the behaviour on the heeled-down side, the spray root speed does not increase with increased flexibility. This asymmetry is likely attributable to the geometry of the problem and the nature of the structural response. On the heeled-up side, the local deadrise angle β_2 is 25°, which is close to the angle at which the spray root departs from the chine following flow separation (approximately 36°, as discussed by Tassin et al.).

The temporal normalised average velocity of the flow along the both side of the wedge is affected by the flexibility. During the early stage of the impact, where a large average velocity emerges, flexibility mitigates the average velocity, but in the last stage of the water entry process, where the whole body of the wedge is about to be fully washed by the water, the normalised average velocity of a flexible case is larger.

The effects of flexibility and elastic modulus on the normalised peak pressure, normalised peak deflection at the midpoint, normalised horizontal spray root speed at the time of maximum pressure, and the normalised maximum equivalent stresses on both the heeled-down and heeled-up sides of the wedge are presented in Fig. 13, for two wedges with deadrise angles of $\beta = 20°$ and $\beta = 30°$.

It is evident that the flexible wedge, whether with $\beta = 20°$ or $\beta = 30°$, experiences lower impact pressures on both the heeled-down and heeled-up sides across all considered water entry speeds, with a few exceptions. In general, a reduction in elastic modulus leads to a decrease in the normalised peak pressure at the middle point across all considered speeds. Yet, an exception is observed on the heeled-up side of the wedge with $\beta = 30°$ (i.e., $\beta_2 = 35°$), where at the two highest entry speeds ($u = 4$ m/s and $u = 5$ m/s), the pressure acting on the wall of the wedge with the lowest elastic modulus exceeds that of the stiffer cases. This anomalous behaviour is likely attributable to the very low stiffness of the structure, which may exhibit significant elastic responses under high impact velocities.

The maximum deflection observed on either side of the elastic wedges is inversely proportional to the elastic modulus, indicating the emergence of solid dynamic responses during the water entry process. As expected, the deflection is significantly smaller for the stiffer panels (i.e., $E = 210$ GPa and $E = 70$ GPa) compared to the more flexible configurations. The normalised horizontal spray root speed at the instant when the peak pressure occurs at the midpoint is only slightly affected by flexibility for both wedge geometries and on both sides. These effects are most pronounced in the case of the highly flexible wedge ($E = 10$ GPa). When the local deadrise angle is approximately 35°, the influence of flexibility on spray root speed becomes less evident. This may reflect a physical consequence of structural deflection, although the possibility of numerical or model-related artefactual effect cannot be entirely ruled out. These observations do not agree with those of Duan et al. (2020), who reported that the propagation speed of the maximum pressure increases with decreasing elasticity. This discrepancy may be attributed to differences between the tests and warrants attention in future work.

The normalised equivalent peak stress at the midpoint of the panels is found to be higher for the elastic wedges with lower elastic modulus, and increases with the increase of water entry speed, u. In contrast, for the stiffer panels, the equivalent peak stress appears to be relatively insensitive to the water entry velocity. This observation is consistent with the trends previously noted in Fig. 9 and Fig. 10.

An index is introduced to quantify the effect of structural flexibility on the peak pressure experienced by heeled wedges during water entry as

$$\tilde{\Delta}\tilde{p}^{\mathrm{f/r}} = \frac{\tilde{p}^{\mathrm{f}}_{\mathrm{MAX}} - \tilde{p}^{\mathrm{r}}_{\mathrm{MAX}}}{\tilde{p}^{\mathrm{r}}_{\mathrm{MAX}}}, \tag{53}$$

where $\tilde{p}^{\mathrm{f}}_{\mathrm{MAX}}$ and $\tilde{p}^{\mathrm{r}}_{\mathrm{MAX}}$ denote the peak normalised pressure at the midpoint of the flexible and rigid wedges, respectively. This index measures the relative reduction (or increase) in normalised peak pressure due to dynamic responses emerging in flexible panels.

Since the change in the horizontal speed of the spray root was observed to be relatively modest in all cases, it is hypothesised that the variation in peak pressure is more strongly influenced by the maximum panel deflection. This deflection may reflect both the work done by the water on the structure during impact and the resulting change in panel geometry,each of which can physically affect the peak pressure. The former may reduce the pressure by attenuating a portion of the energy of water moving towards it through structural deformation, while the latter may do so by locally curving the surface, thereby moderating the hydrodynamic impact load, at least in theory. Accordingly, $\tilde{\Delta}\tilde{p}^{\mathrm{f/r}}$ is plotted against the maximum normalised deflection and presented in Fig. 14.

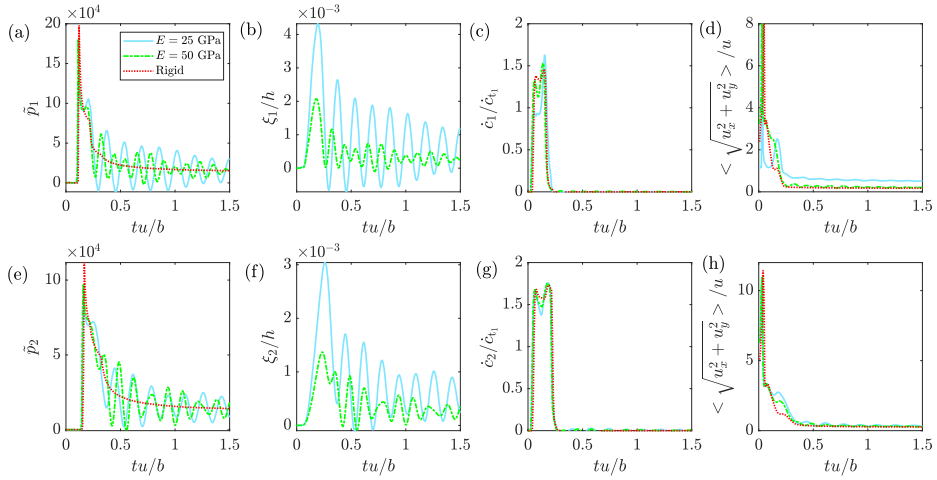

Fig. 12. Effects of panel flexibility in an asymmetric wedge on the evolution of pressure, dynamic response at the midpoint of the panel, spray root velocity on both sides of the wedge, and temporally averaged velocity along the wedge. The upper panels correspond to the heeled-down side, and the lower panels to the heeled-up side. Results are shown for an impact speed of 4 m/s and three configurations: a rigid wedge, an elastic wedge with $E = 25$ GPa, and an elastic wedge with $E = 50$ GPa.

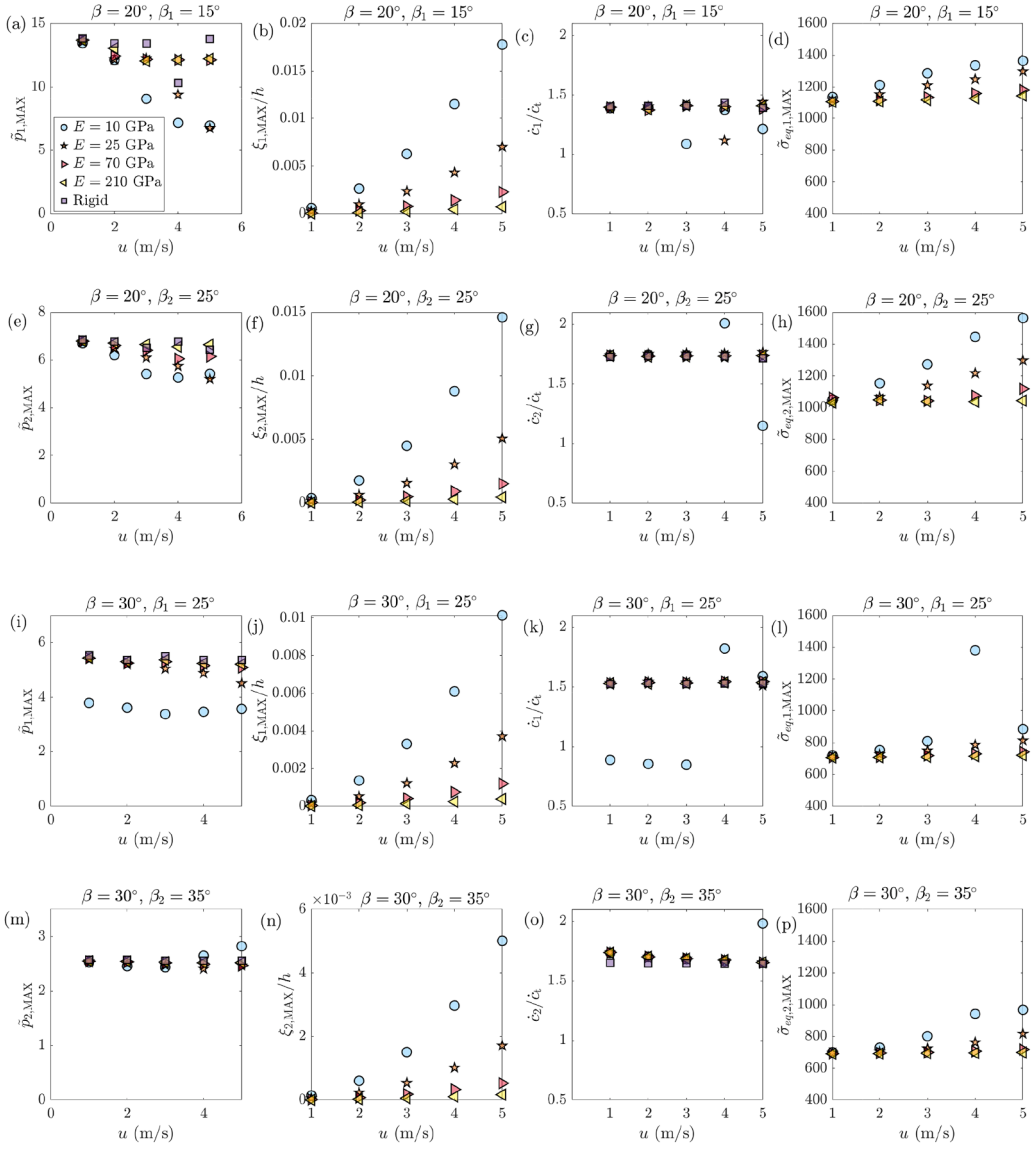

Fig. 13. Effects of flexibility on the normalised peak pressure, deflection, spray root velocity, and peak normalised equivalent stress in the solid body on both the heeled-down and heeled-up sides of two different wedges with deadrise angles of $\beta = 20°$ and $30°$.

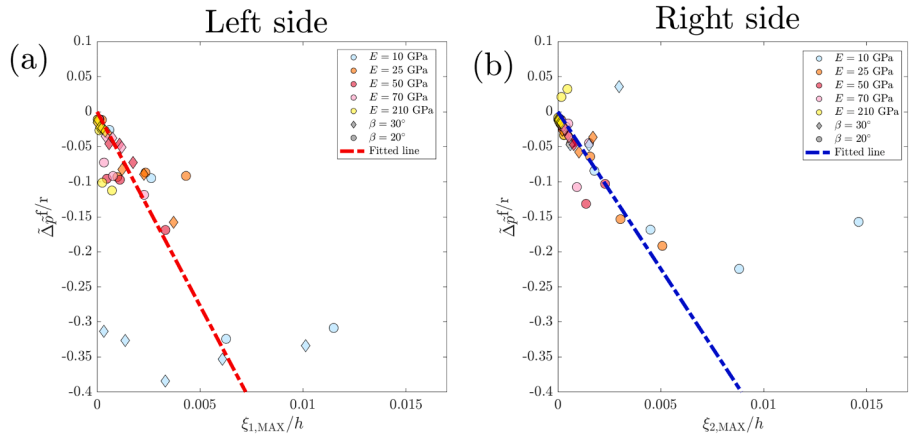

Fig. 14. Relative changes in the peak normalised pressure on the heeled-down and heeled-up sides of a wedge as a function of the maximum deflection on the corresponding side. Curve-fitting lines are included to represent the trend through the data.

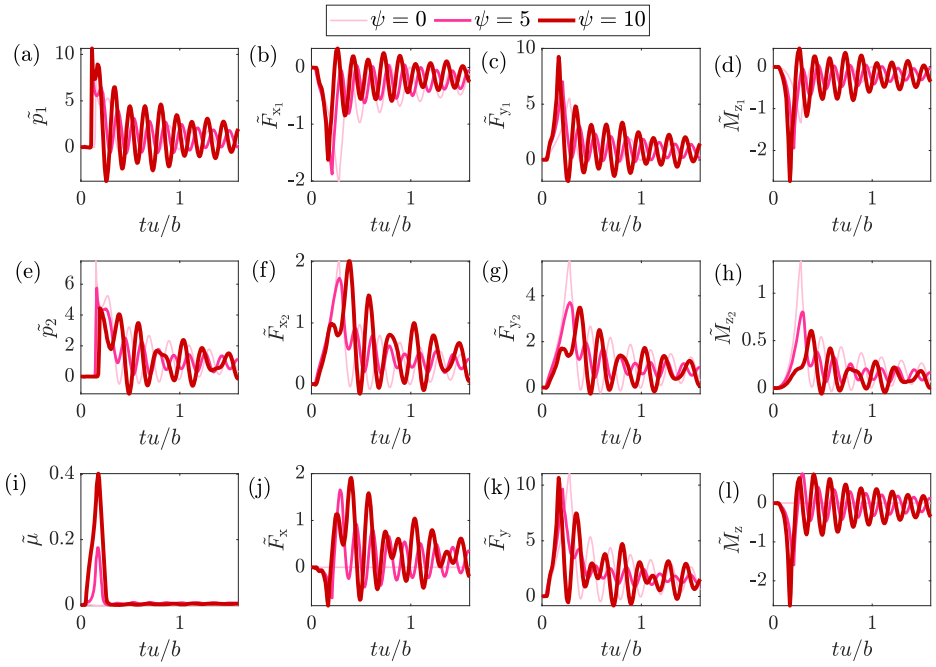

Fig. 15. Effects of heel angle on the time history of pressure at the midpoint of the left and right sides of an asymmetric wedge, along with its influence on the time histories of horizontal force, vertical force, and rolling moment on each side and their total values. Panel (i) shows the temporal evolution of $\tilde{\mu}$, which measures the difference between the wetted beam lengths on each side of the wedge. Results correspond to three different heel angles: $\psi = 0°$, $\psi = 5°$, and $\psi = 10°$, at an impact speed of 4 m/s and for a wedge with an elastic modulus of 25 GPa.

As observed, the normalised peak pressure on both sides of the wedge decreases when the structure exhibits flexible motion, with $\tilde{\Delta p}^{f/r} < 0$ in most cases. The relative reduction in peak normalised pressure at the midpoint is generally proportional to the maximum normalised deflection at that location. However, an exception is noted on the left side of the wedge with $\beta = 30°$ and $E = 10$ GPa, where the relative pressure reduction is approximately 0.35, irrespective of the observed deflection.

Lines consistent with the physical expectations of the problem, namely, that $\tilde{\Delta p}^{f/r} \to 0$ as $\xi_{MAX} \to 0$ and $\tilde{\Delta p}^{f/r} \to -\infty$ as $\xi_{MAX} \to \infty$, can be fitted to the data relating relative pressure reduction to maximum deflection. On the left side (the heeled-down side), the slope of the fitted line is approximately −0.55, while on the right side (the heeled-up side), it is approximately −0.45. This trend is physically reasonable, given that the local deadrise angles on the left side are $\beta_1 = 15°$ and $\beta_1 = 25°$, whereas on the right side, the angles are $\beta_2 = 25°$ and $\beta_2 = 35°$. Since lower deadrise angles are generally associated with more pronounced pressure reductions under flexible response, the steeper slope observed on the left side is consistent with expectations.

5.3. Effects of heel angle

The results of the test matrix outlined in Table 3 are analysed in this subsection to provide an understanding of the effects of heel angle on the dynamic response of the flexible wedges entering the water. To analyse the data, the force acting on the flexible wedge is computed as

$$\boldsymbol{F} = \int_{\Gamma_{FSI}} (-p\,\boldsymbol{n} + \boldsymbol{\tau} \cdot \boldsymbol{n})\, dA, \tag{54}$$

where the first component of $\boldsymbol{F}$ is the horizontal force acting on the section, and the second component is the vertical force. If the calculation

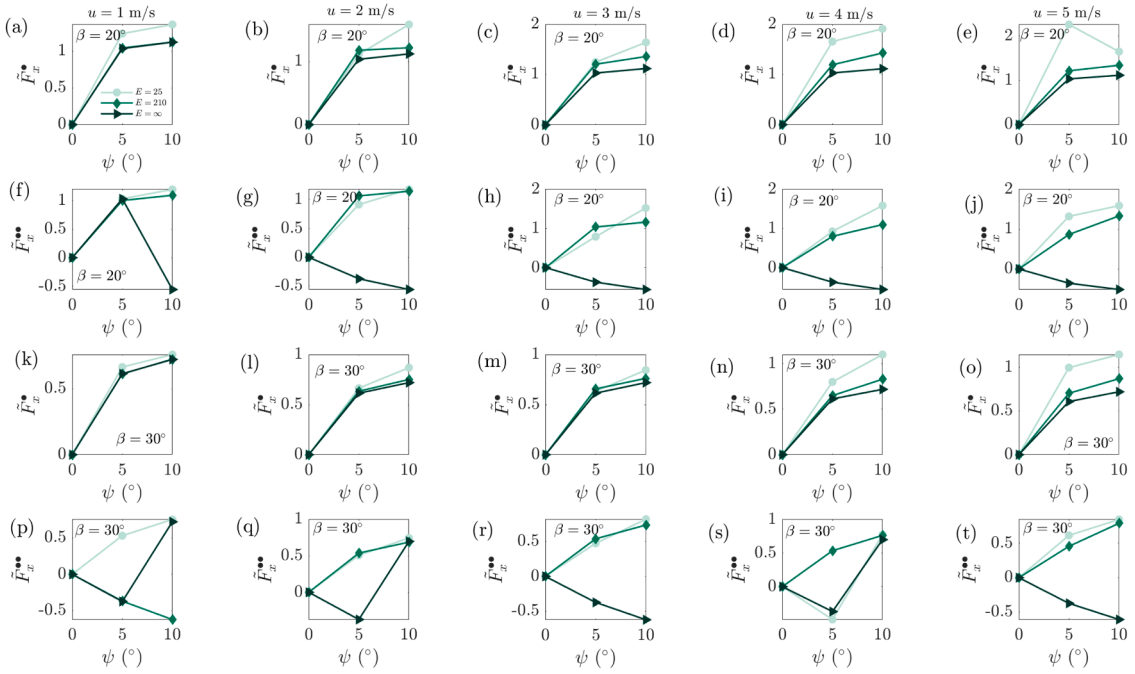

Fig. 16. Largest and second-largest peaks observed in the time history of the normalised horizontal force ($\tilde{F}_x$) as a function of heel angle, evaluated at different impact speeds for two wedge geometries. Results are shown for a rigid wedge and two flexible wedges with elastic moduli of $E = 25$ GPa and $E = 210$ GPa.

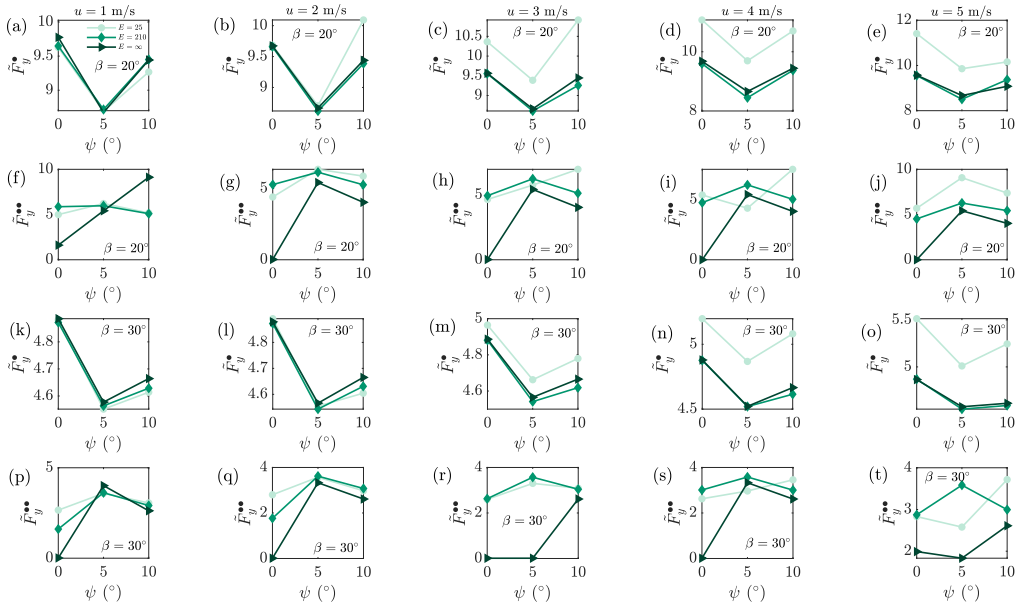

Fig. 17. Largest and second-largest peaks observed in the time history of the normalised vertical force ($\tilde{F}_z$) as a function of heel angle, evaluated at different impact speeds for two wedge geometries. Results are shown for a rigid wedge and two flexible wedges with elastic moduli of $E = 25$ GPa and $E = 210$ GPa.

is carried out for $x < 0$, it yields the force acting on the heeled-down side of the wedge (for $\psi \neq 0$), while evaluation over $x > 0$ gives the force acting on the heeled-up side. For the case $\psi = 0$, no heel is present, and such terminology does not apply; however, the horizontal forces acting on $x < 0$ and $x > 0$ are equal in magnitude and opposite in direction, and thus cancel each other. The moment acting on the section is calculated as

$$\boldsymbol{M} = \int_{\Gamma_{\mathrm{FSI}}} \mathbf{x} \times (-p\,\mathbf{n} + \tau \cdot \mathbf{n})\, dA. \tag{55}$$

All components of $\boldsymbol{M}$ are zero except the last, which corresponds to the rolling moment. As with the force, if the integral in Eq. 56 is evaluated over $x < 0$, the moment acting on the heeled-down side is obtained; if evaluated over $x > 0$, the moment acting on the heeled-up side is found.

The force components and roll moment acting on the wedge are normalised as

$$\tilde{F}_{\mathrm{x}} = \frac{F_{\mathrm{x}}}{\rho_{\mathrm{water}} u^2 B}, \quad \text{and} \quad \tilde{F}_{\mathrm{y}} = \frac{F_{\mathrm{y}}}{\rho_{\mathrm{water}} u^2 B}, \quad \text{and}$$
$$\tilde{M}_{\mathrm{y}} = \frac{M_{\mathrm{y}}}{\rho_{\mathrm{water}} u^2 B^2}. \tag{56}$$

A parameter measuring the difference between the half-wetted beam on the heeled-up and heeled-down sides of the wedge is also introduced,

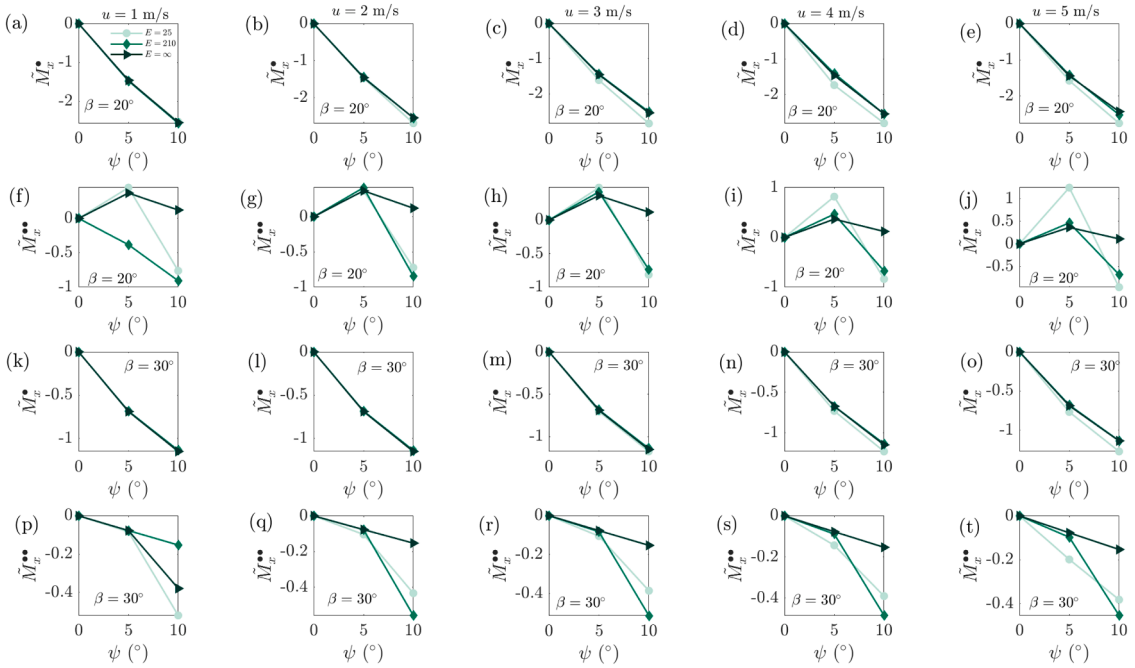

Fig. 18. Largest and second-largest peaks observed in the time history of the rolling moment $\tilde{M}_z$ as a function of heel angle, evaluated at different impact speeds for two wedge geometries. Results are shown for a rigid wedge and two flexible wedges with elastic moduli of $E = 25$ GPa and $E = 210$ GPa.

defined as

$$\mu = c_1 - c_2. \tag{57}$$

Fig. 15 shows the time histories of the normalised peak pressure, horizontal and vertical forces, roll moment, and μ for a flexible wedge with a deadrise angle of $\beta = 20°$ at three different heel angles: $\psi = 0°$, $\psi = 5°$, and $\psi = 10°$. These cases correspond to an impact speed of $u = 4$ m/s, and the elastic modulus of the panel is $E = 25$ GPa. In this figure, increasing heel angles are represented by progressively thicker and darker curves within a pink colour range.

As seen, the heel angle can affect the hydrodynamic pressure and the loads acting on a heeled wedge. On the heeled-down side of the wedge, where the local deadrise angle decreases with increasing ψ, both the peak normalised pressure and the second peak, associated with the dynamic response, are observed to increase with heel angle. This trend aligns with physical expectations; that is, for a smaller deadrise angle, a larger dynamic pressure is expected to develop on the wedge wall during the water-entry process. The opposite behaviour is observed on the heeled-up side of the wedge, as the change in local deadrise angle is reversed; consequently, the peak normalised pressure is expected to decrease with increasing heel angle.

The horizontal force acting on the left side of the wedge is initially negative and increases until it reaches a negative peak, which corresponds to the instant of water detachment from the left chine. The magnitude of this negative peak is observed to decrease with increasing heel angle. Following flow separation, F_{x_1} exhibits a harmonic behaviour that decays over time. However, the amplitude of the temporal variation in force is larger for the case with a greater heel angle, due to the larger dynamic responses arising for a wedge with a larger heel angle.

On the heeled-up side of the wedge, however, the effect of heel angle on the horizontal force is different. This force component is positive on the right side of the wedge and increases until it reaches a peak value, which again corresponds to the instant of water detachment from the chine. As observed, when the heel angle increases from $\psi = 0°$ to $\psi = 5°$, the peak horizontal force decreases, despite the increase in the local normal unit vector (i.e., $\sin\beta_i$). However, as the heel angle increases further from $\psi = 5°$ to $\psi = 10°$, the peak horizontal force increases. This indicates a nonlinear dependence of the horizontal force on ψ.

Interestingly, the amplitude of oscillation in the horizontal force on the heeled-up side, immediately following flow separation from the chine, initially decreases as the heel angle increases from $\psi = 0°$ to $\psi = 5°$, but then increases again as the heel angle increases from $\psi = 5°$ to $\psi = 10°$. This trend may be attributed to the contribution of a second mode in the dynamic response of the wedge. As observed, more than one harmonic appears to contribute to the dynamic response on the right side of the wedge for $\psi = 10°$, suggesting the possible occurrence of resonance.

As can be observed, the magnitude of both the first and second peaks of the total horizontal force acting on the wedge increases with increasing heel angle. Moreover, the response associated with the second-lowest mode is also seen to influence the resulting horizontal force when $\psi = 10°$.

The vertical force acting on both the left and right sides of the wedge is observed to increase until reaching a peak, after which it decreases and is followed by a decaying response. This peak corresponds to the moment of water separation from the chine on the respective side. On the heeled-down side, an increase in ψ leads to an increase in the magnitude of the positive peak of vertical force, as well as in the amplitude of the subsequent oscillations. This behaviour closely matches that observed for the normalised pressure. On the heeled-up side of the wedge, it is evident that increasing the heel angle leads to a reduction in the vertical force. However, the extent of this reduction becomes less significant with further increases in heel angle. Similar to the behaviour observed for the horizontal force on the right side, the modal response associated with the second mode may also influence the time history of the vertical force when $\psi = 10°$. The total vertical force is generally observed to decrease as the heel angle increases from $\psi = 0°$ to $\psi = 5°$, and then to increase as the heel angle rises from $\psi = 5°$ to $\psi = 10°$.

The rolling moments acting on the left and right sides of the wedge entering water are observed to follow similar trends to those of the vertical and horizontal forces until water detachment occurs, with the rolling moment on the heeled-down side of the wedge being negative, and that on the heeled-up side being positive. On the left side, a heeled-down condition increases the magnitude of the peak occurring just before water detachment. In contrast, on the right side, increasing the heel angle

leads to a reduction in the magnitude of the first peak. This highlights the clear effect of the local deadrise angle, for lower values of which, a larger rolling moment is expected to develop on the wedge wall during the water-entry process prior to flow separation.

Following the water detachment, the amplitude of rolling moment oscillations on the left side is seen to be larger for cases with greater heel angle. On the right side, the amplitude of oscillation initially decreases as the heel angle increases from $\psi = 0°$ to $\psi = 5°$, and then increases as the heel angle rises from $\psi = 5°$ to $\psi = 10°$. This trend is consistent with the observations made for the vertical and horizontal forces on the right side and provides strong support for the hypothesis that the second mode contributes to the dynamic response in the case with $\psi = 10°$. The total rolling moment acting on the elastic wedge is seen to be influenced by the increase in heel angle, and equals nil for the case with $\psi = 0$.

Interestingly, in the time-history plots of the total horizontal force, vertical force, and rolling moment acting on the wedge, two remarkable peaks can be identified. One may correspond to the instant of water detachment from one side of the wedge, while the other may be associated with the dynamic response of the elastic panel.

Finally, it should be noted that the difference between the half-wetted beam on the heeled-down side and that on the heeled-up side is observed to increase over time until flow separation occurs on one side. It then decreases and eventually approaches zero, once the heeled-up side becomes fully wetted.

The effects of heel angle on the forces and moment acting on flexible and rigid wedges at different impact speeds are shown in Figs. 16, 17 and 18. The elasticity of the model is indicated using shades of green, with lighter shades representing lower elastic moduli and darker shades corresponding to the rigid case. For each force and moment, two values denoted by superscripts • and •• are identified and plotted as a function of heel angle. The values marked with • correspond to the largest recorded peak, while those marked with •• represent the second-largest peak. The first two rows of each Figure show the data corresponding to $\beta = 20°$, and the second two rows show the data for $\beta = 30°$, with the value of β indicated as text within each panel. Each column presents the data corresponding to a different impact speed, u.

As observed, the first peak of the normalised horizontal force, $\tilde{F}_x^{\bullet}$, for both flexible and rigid wedges increases with heel angle, but this increase is nonlinear. Notably, the peak value $\tilde{F}_x^{\bullet}$ is larger for more flexible wedges, i.e., those with a lower elastic modulus. The second peak of the normalised horizontal force, $\tilde{F}_x^{\bullet\bullet}$, also exhibits a nonlinear dependence on heel angle. However, for the highly flexible case ($E = 25$ GPa), this second peak increases almost linearly with heel angle in most of cases. Interestingly, the trend of $\tilde{F}_x^{\bullet\bullet}$ as a function of heel angle in flexible wedges may be opposite to that observed in rigid wedges. This contrasting behaviour provides direct evidence that dynamic responses of the wedge panel during water entry can significantly alter the force distribution. Such effects may influence the whipping force experienced by a vessel in waves, particularly when local panel flexibility leads to dynamic slamming responses.

Moreover, the second-largest peak of horizontal force, $\tilde{F}_x^{\bullet\bullet}$, is comparable in magnitude to the first peak, $\tilde{F}_x^{\bullet}$, highlighting the importance of accounting for this secondary peak when estimating the horizontal moment acting on a vessel during slamming events.

The largest peak of the slamming force, $\tilde{F}_y^{\bullet}$, acting on the wall of the wedge is also clearly influenced by heel angle for both considered deadrise angles. It increases with heel angle from $\psi = 0°$ to $\psi = 5°$, and continues to increase from $\psi = 5°$ to $\psi = 10°$. The $\tilde{F}_z^{\bullet}$ versus ψ curves for the rigid wedge and the wedge with $E = 210$ GPa closely follow each other, while the corresponding curve for the wedge with $E = 25$ GPa deviates from these, indicating a notable influence of flexibility on the slamming response.

The second-largest peak of the normalised vertical force, $\tilde{F}_y^{\bullet\bullet}$, also exhibits nonlinear behaviour under variations in heel angle. It generally increases with heel angle from $\psi = 0°$ to $\psi = 5°$, and then decreases as the heel angle increases from $\psi = 5°$ to $\psi = 10°$ in most cases. Interestingly, the rigid wedge experiences the most significant change in $\tilde{F}_y^{\bullet\bullet}$ between $\psi = 0°$ and $\psi = 5°$, as compared to the elastic wedges.

Another notable observation is that the values of $\tilde{F}_y^{\bullet\bullet}$ are approximately half of the corresponding first peak and are non-zero even at zero heel angle for the elastic cases. This clearly supports the notion that elastic effects should be considered in the calculation of whipping forces.

The largest peak value of the normalised rolling moment, $\tilde{M}_z^{\bullet}$, is observed to increase with heel angle, with the increase being nearly linear. However, the slope of this increase decreases as the heel angle becomes larger. The slope of the $\tilde{M}_z^{\bullet}$ versus heel angle curves is slightly greater for the wedge with lower stiffness compared to the stiffer and rigid wedges. This observation strongly supports the idea that the rolling moment of a flexible wedge is influenced by its dynamic responses.

The second-largest peak value of the normalised rolling moment, $\tilde{M}_z^{\bullet\bullet}$, shows different trends depending on the wedge configuration. For the wedge with a deadrise angle of $\beta_1 = 20°$, $\tilde{M}_z^{\bullet\bullet}$ first takes a positive value as the heel angle increases from $\psi = 0°$ to $\psi = 5°$, and then becomes negative as the heel angle increases from $\psi = 5°$ to $\psi = 10°$. These changes are more significant for the elastic cases, particularly for the wedge with the lowest elastic modulus, which exhibits the largest variations in $\tilde{M}_z^{\bullet\bullet}$ with increasing heel angle. This behaviour is likely linked to the dynamic response of the panel. For the other deadrise angle, i.e., $\beta_2 = 30°$, $\tilde{M}_z^{\bullet\bullet}$ is negative for all heel angles and becomes more negative as the heel angle increases from $\psi = 0°$ to $\psi = 5°$, and then to $\psi = 10°$.

6. Conclusions

In this study, aiming to address the existing knowledge gap, asymmetric flexible water entry was modelled using an open-source coupled CFD–CSD code. It was demonstrated that the asymmetric flow pattern significantly influences the hydrodynamic pressure and the resulting dynamic responses by decelerating the spray root on the heeled-down side of the wedge and accelerating it on the heeled-up side, relative to a symmetric wedge with comparable local deadrise angles. These changes in spray root dynamics were found to be proportional to variations in the impact pressure.

In addition, by modelling the problem for different heeled wedge configurations, the dynamic responses and pressures acting on the structure were numerically evaluated. It was concluded that the impact pressure is generally reduced when the panel is flexible, compared to the rigid panel assumption. This reduction was found to exhibit a linear relationship with the maximum deflection occurring in the structure. This well shows that dynamic response, which may take some of the fluid energy, and also may change the instant geometry of the structure, can cause changes in impact pressure.

It was also observed that the heel angle influences the vertical and horizontal forces, as well as the rolling moment acting on the wedge, with two distinct peaks appearing in the time histories of these quantities. The largest and second-largest values of the forces and moment were found to depend on heel angle in a nonlinear manner, suggesting that the nonlinearity associated with fluid velocity and the dynamic response of the structure can significantly influence the resulting whipping forces and moments. Consequently, rigid-body models or those that neglect fluid and structural nonlinearities may not be suitable for accurately predicting whipping loads acting on ships in oblique or beam seas, which are common in real maritime environments.

The present CFD–CSD model resolves the local flexible slamming behaviour of an elastic wedge, and the hydrodynamic and structural responses are expressed entirely in non-dimensional form. This permits the findings to remain applicable across different geometric scales. Although the simulations focus on a small wedge section with a half-beam of 0.5 m, the non-dimensional peak pressure, normalised deflection, and stiffness ratio produce transferable relationships that can be used in larger-scale hydroelastic analyses. In particular, the link

identified here between flexibility-induced pressure changes and the resulting non-dimensional displacement can be scaled to full-size panels in marine structures.

In addition, the dimensionless vertical and horizontal forces and rolling moments obtained for heeled flexible wedges can be incorporated into weakly nonlinear strip-theory models used for simulating global ship hydroelasticity, replacing the rigid water entry models commonly used in existing whipping models (e.g. Peddamallu et al. (2025)). That is, the present CFD–CSD framework provides a physics-based pathway for representing local structural flexibility within global hydroelastic solvers.

A further step, identified as future work, is to express the present results in terms of the non-dimensional momentum exchange between the fluid and the structure (a further extension of the von Kármán (1929) method to account for structural flexibility). This requires developing an asymptotic formulation in which the principal input is the momentum exchange between the fluid and the solid, similar in spirit to the approach of Tavakoli et al. (2023b) which is developed for flat plate water entry. The momentum exchange itself may be expressed as a function of the non-dimensional impact velocity and the non-dimensional stiffness. This can be regarded as a natural next step of the present study. It would yield more general expressions for the slamming force, impact pressure and structural deflections, permitting rapid estimates of these quantities to be incorporated into any two-dimensional strip-theory model that can be run for a real scale, or used directly to calculate design pressures for panels in the bow region subjected to slamming, without the need for full CFD–CSD simulations.

The present CFD–CSD model has an inherent limitation when modelling the dynamic response of flexible panels with simply supported ends subjected to slamming loads. Owing to the nature of the solid solver, the model effectively represents a stiffer panel when applied to cases with simple supports and therefore requires the use of a reduced effective elastic modulus. In contrast, the model can reliably predict the response of panels with two clamped ends. Consequently, the scope of the conclusions made in the present research is restricted to flexible panels with clamped boundary conditions. A further limitation of the present CFD-CSD is that the model has been developed for two-dimensional problems. Yet, three-dimensional effects are expected to influence both the fluid dynamics (Wang et al. (2021)) and the flexible fluid–structure interaction response (Hosseinzadeh et al. (2023b)). As such, further development of the model to address the three-dimensional water-entry problem may be pursued in future work. Given these limitations, the present model could still serve as a candidate for a benchmarking study within the Sea Loads Technical Committee of the ISSC2028, should benchmarking of slamming loads be undertaken.

While the understanding of the hydrostructural behaviour of flexible wedges entering water has advanced, several open questions remain. One such question concerns the case where flow separation occurs at the apex of the wedge, which may arise at large heel angles. This condition can result in a substantially different flow pattern during water entry. An important direction for future research is the modelling of oblique water entry, where an additional velocity component is introduced. This introduces further complexity into the nonlinear fluid–structure interaction, particularly in the near-wall region of the wedge.

CRediT authorship contribution statement

Sasan Tavakoli: Writing – review & editing, Writing – original draft, Visualization, Validation, Software, Methodology, Investigation, Formal analysis, Conceptualization; **Saeed Hosseinzadeh:** Writing – review & editing, Investigation, Formal analysis, Conceptualization; **Theodosis D. Tsaousis:** Writing – review & editing, Investigation, Formal analysis, Conceptualization; **Spyros Hirdaris:** Conceptualization, Supervision, Writing – review & editing.

Declaration of competing interest

The authors declare the following financial interests/personal relationships which may be considered as potential competing interests:

Sasan Tavakoli and Spyros Hirdaris are Editorial Board Members of Ocean Engineering. The authors declare that there are no other known competing financial interests or personal relationships that could have appeared to influence the work reported in this paper.

Appendix A. Mesh sensitivity

The sensitivity of the results to cell size was examined by running one case ($\beta = 20°$, $\psi = 5°$, $u = 4$ ms^{-1}) with four different mesh resolutions: coarse, medium, fine and very fine. The cell size was varied by adjusting N_x and N_y in the block adjacent to the fluid–solid interface. For the coarse mesh, $N_x = 50$, while for the very fine mesh, $N_x = 120$. The maximum pressure and deflection at a point on the left side of the wedge, where the local deadrise angle is 15°, were monitored, and the results obtained from each model are plotted in Fig. 19. As seen, the maximum pressure results are less sensitive to cell size when a medium mesh is employed, although the deflection results still show some sensitivity. Accordingly, the fine mesh was selected for the simulations presented in this paper.

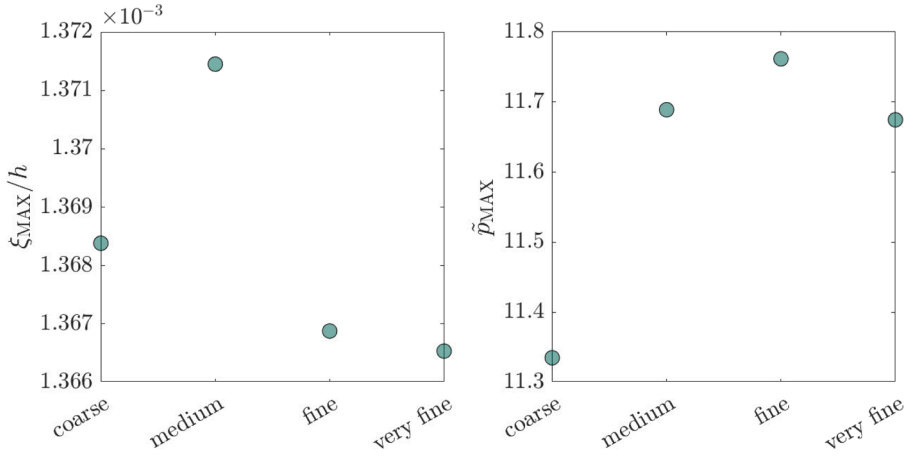

Fig. 19. Mesh sensitivity results.

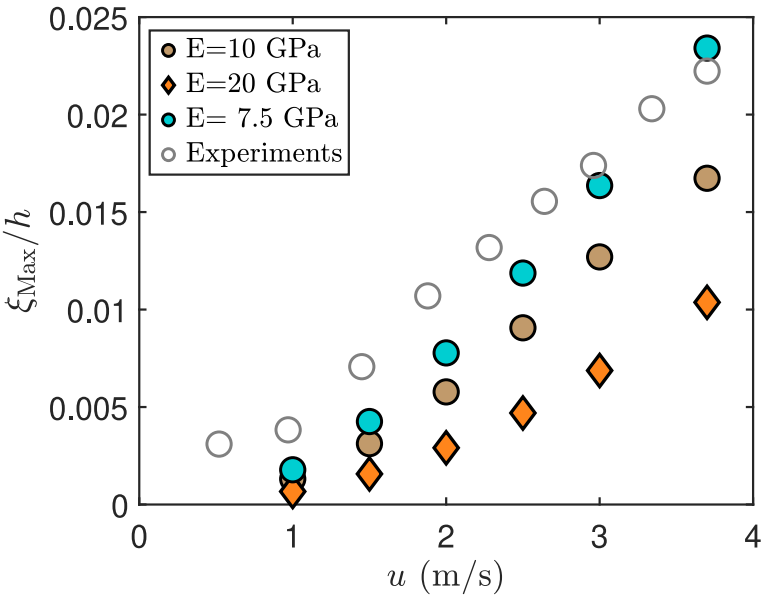

Fig. B.20. Comparison between the maximum midspan deflection obtained from experiments and numerical simulations for a 10° elastic wedge entering water at different impact speeds.

Appendix B. Model Comparison: Maximum deflection of flexible panel with simply supported ends (experimental data)

In this appendix, the numerical results are compared against the experiments of Stenius et al. (2013), who investigated the dynamic response of wedges entering water with a deadrise angle of 10°. The tests were conducted at different impact velocities, and the maximum deflection at the midspan was recorded. Corresponding numerical simulations were performed; however, the present model cannot be expected to replicate the experiments exactly owing to certain limitations. The experimental model consists of flexible edges near the wedge apex and chines, which resemble a simply supported boundary condition (Battley and Allen (2012)), but this configuration cannot be modelled computationally using the present CFD–CSD framework. Hence, the panel simulated in the CFD–CSD model when used for modelling simply supported panels is stiffer. As a result, the CFD–CSD framework cannot reproduce the experimental results when using the same elastic modulus. Similar, though not identical, trends can only be obtained by assigning a lower effective elastic modulus in the simulations. To assess sensitivity, different elastic moduli were prescribed for the structure: $E = 20$ GPa, $E = 10$ GPa and $E = 7.5$ GPa, the former of which equals that of the material tested in experiments. The highest modulus corresponds to that of the material employed in the experiments.

As seen (Fig. B.20), the results of the present CFD-CSD model acquired for $E = 20$ GPa are smaller than those measured in the experiments. This is not surprising, as the present model cannot represent simply supported ends. However, the agreement improves as the elastic modulus is reduced. This indicates that the model can reproduce the dynamic response of panels with simply supported ends subjected to slamming loads, provided that the elastic modulus is chosen appropriately. This is because the stiffness of a panel with two clamped ends, as modelled here, is four times greater than that of a panel with simple supports. This is a limitation of the present model.

Appendix C. Model comparison: Temporal maximum strain of a flexible panel with simply supported ends (Wagner-based model)

The numerical results of the present CFD–CSD model are also compared with the predictions of the coupled Wagner-based model developed by Khabakhpasheva and Korobkin (2013). The wall of the wedge

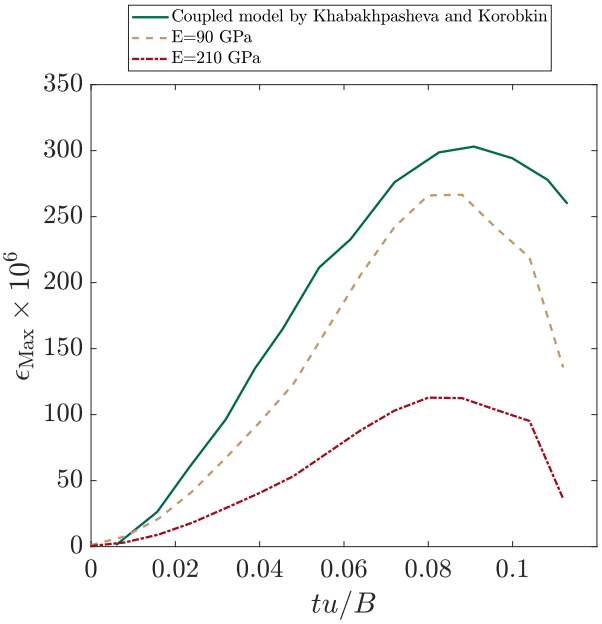

Fig. C.21. Comparison between the starin arising at the midspan deflection obtained from experiments and numerical simulations for a 10° elastic wedge entering water at different impact speeds.

was idealised as a simply supported beam, a boundary condition that the present CFD–CSD solver cannot represent. An elastic steel wedge entering water at an impact velocity of 4 m/s, with a panel thickness of 24 mm. Since the present model is expected to idealise a stiffer panel than that in Khabakhpasheva and Korobkin (2013), different elastic moduli are examined, namely $E = 20$ GPa, $E = 90$ GPa It should also be noted that the present CFD–CSD model is not expected to reproduce the results of the Wagner-based model developed by Khabakhpasheva and Korobkin (2013), as their formulation idealises an elastic beam with two simply supported ends by setting the Elastic modulus set by Khabakhpasheva and Korobkin (2013), whereas the present framework models a

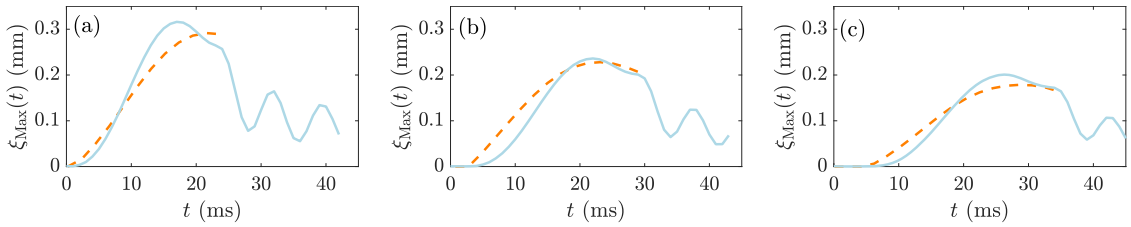

Fig. D.22. Comparison between the maximum temporal deflection in the flexible panel of a wedge with a deadrise angle of $\beta = 20°$ obtained from experiments (dashed curves) and CFD–CSD simulations (solid curves). Panels (a), (b) and (c) respectively show the results for impact speeds of 3 m/s, 2.6 m/s and 2.4 m/s.

panel with two clamped ends. As discussed in Appendix B, this distinction represents an inherent limitation of the current model.

The maximum equivalent stresses in the panel are extracted and compared with those predicted by Khabakhpasheva and Korobkin (2013), as shown in Fig. C.21. The present numerical predictions broadly follow the trends of the Wagner-based model. However, the results diverge when the elastic modulus in the CFD–CSD model is set equal to that used in Khabakhpasheva and Korobkin (2013), and the agreement improves as the modulus is reduced. This behaviour arises because, as explained in Appendix A, simply supported boundary conditions cannot be imposed in the present model, and the stiffness of the modelled plate is therefore expected to be greater than the one modelled by Khabakhpasheva and Korobkin (2013).

Appendix D. Model comparison: Temporal maximum deflection of the flexible panel with clamped end (experimental data)

In this appendix, the results of the present CFD–CSD model are compared with the experimental measurements of Gilbert et al. (2023), who reported the hydroelastic response of elastic wedges entering water. The edges of the tested panels are mechanically closer to clamped conditions, unlike those in the experiments of Battley and Allen (2012), Stenius et al. (2013). Consequently, comparing the predicted panel displacements from the present model with the measured displacements offers a clearer assessment of the accuracy level of the present CFD-CSD model in resolving the displacement field of a panel subjected to slamming. Here, the response of an elastic wedge with $b = 0.3$ m, thickness $h = 9.5$ mm, and elastic modulus $E = 18$ GPa is numerically modelled. The tests were performed at three different impact speeds, $u = 2.4$, 2.6, and 3 m/s. Gilbert et al. (2023) reported the temporal maximum deflection recorded in the elastic panel, ξ_{Max}. Accordingly, the maximum value at each time step is monitored and compared against the experimental values, as shown in Fig. D.22.

As seen, the results of the computational model (solid curves) follow the experimental data (dashed curves) at all three tested speeds, with the maximum detected displacement from the CFD–CSD model being close to the experimentally recorded values. Unlike what was observed in Appendices B (comparisons against experimental measurements of Stenius et al. (2013)) and C (comparisons against numerical predictions of the Wagner-based model of Khabakhpasheva and Korobkin (2013)), the CFD–CSD model predicts similar results to the experiments using the same elastic modulus of the panel. This agreement is mainly due to the nature of the model and the experimental setup. As explained earlier, the present computational model can only be constructed for clamped boundary conditions, and the setup in the experiments of Gilbert et al. (2023) closely resembles clamped boundary conditions at both the wedge apex and near the chine, as opposed to the experimental and numerical setups of Stenius et al. (2013) and Khabakhpasheva and Korobkin (2013).

Appendix E. Model Comparison: Rigid wedge pressures (experimental, numerical and analytical models)

The level of the accuracy of the model in the prediction of the pressure acting on the wedge entering water is also evaluated by comparing its predictions against those of experimental measurements and what previous analytical and numerical potential-based flow models give. Yet, this comparison is carried out only for the rigid wedge configuration. This is intentional, as it allows verification that the model can accurately predict the pressure acting on a rigid wedge.

At a first step, the pressure distribution along the wall of three different rigid wedges with $\beta = 15°$, 20°. and 25° are computed and compared against experiments of Yettou et al. (2006). The CFD simulations were performed for a wedge with $b = 0.6$ m and an impact speed similar to that of the experiments, $u \approx 4.5$ m/s. Fig. D.23 shows a comparison between the pressure distribution measured in the experimental tests of Yettou et al. (2006) and that obtained from the CFD model for the rigid configuration. As seen, the CFD model reproduces a pressure distribution similar to that observed in the experiments, with the peak value and the pressure near the wedge apex in very close agreement. A difference of up to approximately 10 % is observed between the numerical and experimental results in the predicted values near the midpoint of the wetted area.

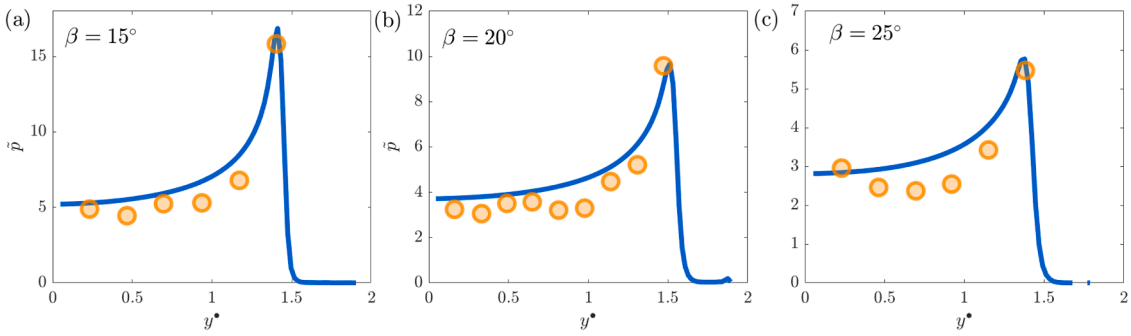

Fig. D.23. Comparison between the predicted pressure distribution along the wall of rigid wedges (solid curves) and the experimentally measured values of Yettou et al. (2006) (circle markers). Panels (a), (b) and (c) show the results for wedge sections with deadrise angles of $\beta = 15°$, $\beta = 20°$ and $\beta = 25°$, respectively.

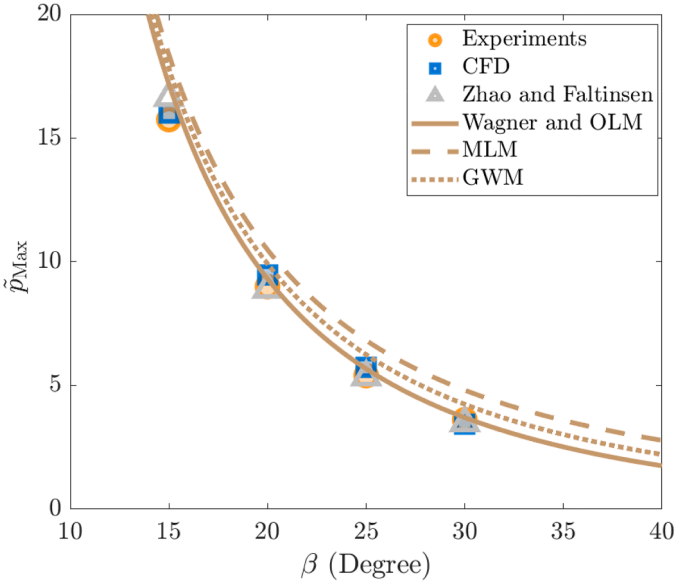

Fig. E.24. Maximum normalised pressure versus deadrise angle of symmetric rigid wedges obtained from the present CFD model, compared with the experimental results of Yettou et al. (2006), the numerical simulations of Zhao and Faltinsen (1993), and the analytical predictions from the OLM, MLM, and GWM models.

In the next step, the maximum pressure values obtained from the CFD simulations with the rigid setup are compared against those from the experiments. In addition, the maximum pressures predicted by three analytical models presented in Korobkin (2004) are also calculated. These models are referred to as the Original Logvinovich Model (OLM), the Modified Logvinovich Model (MLM), and the Generalised Wagner Model (GWM). The maximum pressures given by these models are

$$p_{\mathrm{MAX}} = \frac{1}{2}\rho \dot{c}^2 \qquad \text{(OLM)}, \qquad \text{(E.1)}$$

$$p_{\mathrm{MAX}} = \frac{1}{2}\rho \dot{c}^2 \left[\cos^{-2}\beta - \frac{u^2}{\dot{c}^2}\sin^2\beta\right] \qquad \text{(MLM)}, \qquad \text{(E.2)}$$

$$p_{\mathrm{MAX}} = \frac{1}{2}\rho \dot{c}^2 \left[\cos^{-2}\beta - \frac{u^2}{\dot{c}^2}\left(\sin^2\beta + \pi - 2\right)\right] \qquad \text{(GWM)}, \qquad \text{(E.3)}$$

where $\dot{c}$ is found using Eq. 48.

Fig. E.24 shows the maximum values of the normalised pressure obtained from the present CFD model, those reported in the experiments of Yettou et al. (2006), the analytical predictions from the OLM, MLM, and GWM models, and the numerical results of Zhao and Faltinsen (1993) for a rigid wedge with different deadrise angles. Evidently, the maximum normalised pressure predicted by the present CFD model is close to that measured experimentally. In particular, its predictions are more accurate than those of Zhao and Faltinsen (1993) for $\beta = 15°$. The OLM model is also seen to provide the closest maximum normalised pressure to both the experimental data and the present CFD predictions.

References

Aagaard, O., 2013. Hydroelastic Analysis of Flexible Wedges. Master's thesis. Norwegian University of Science and Technology (NTNU). Trondheim, Norway. Supervisors: Bernt Johan Leira, Bjørnar Pettersen, Svein Erling Heggelund.

Aitken, A., 1926. On bernoulli's numerical solution of algebraic equations. Proc. R. Soc. Edinburgh 46, 289–305. https://doi.org/10.1017/S0370164600022070

Alaoui, A. E.M., Nême, A., Scolan, Y.M., 2015. Experimental investigation of hydrodynamic loads and pressure distribution during a pyramid water entry. J. Fluid. Struct. 54 (4), 925–935.

Amouzadrad, P., Mohapatra, S.C., Guedes Soares, C., 2025. Review on sensitivity and uncertainty analysis of hydrodynamic and hydroelastic responses of floating offshore structures. J. Mar. Sci. Eng. 13 (6), 1015. https://doi.org/10.3390/jmse13061015

Battistin, D., Iafrati, A., 2003. Hydrodynamic loads during water entry of two-dimensional and axisymmetric bodies. J. Fluid. Struct. 17 (5), 643–664. https://doi.org/10.1016/S0889-9746(03)00021-3

Battley, M., Allen, T., 2012. Servo-hydraulic system for controlled velocity water impact of marine sandwich panels. Exp. Mech. 52, 95–106. https://doi.org/10.1007/s11340-011-9543-7

Bureau Veritas Marine & Offshore, 2025. Rules for the Classification of Steel Ships: Part B – Hull and Stability. Bureau Veritas. Paris, France. nr467. Available at: https://marine-offshore.bureauveritas.com/nr467.

Chen, Z., Jiao, J., Chang, X., Ma, B., 2024. Numerical and experimental study of asymmetrical wave loads and hydroelastic responses of ship in oblique regular waves. Appl. Ocean Res. 153, 104254. https://doi.org/10.1016/j.apor.2024.104254

Datta, N., Siddiqui, M.A., 2016. Hydroelastic analysis of axially loaded timoshenko beams with intermediate end fixities under hydrodynamic slamming loads. Ocean Eng. 127, 124–134. https://doi.org/10.1016/j.oceaneng.2016.09.039

Datta, N., Troesch, A.W., 2012. Dynamic response of kirchhoff's plates to transient hydrodynamic impact loads. Mar. Syst. Ocean Technol. 7, 79–94. https://doi.org/10.1007/BF03449302

Duan, L., Zhu, L., Chen, M., Pedersen, P.T., 2020. Experimental study on the propagation characteristics of the slamming pressures. Ocean Eng. 217, 107868. https://doi.org/10.1016/j.oceaneng.2020.107868

Facci, A.L., Panciroli, R., Ubertini, S., Porfiri, M., 2015. Assessment of PIV-based analysis of water entry problems through synthetic numerical datasets. J. Fluid. Struct. 55, 484–500. https://doi.org/10.1016/j.jfluidstructs.2015.03.018

Faltinsen, O.M., 2000. Hydroelastic slamming. J. Mar. Sci. Technol. 5, 49–65.

Faltinsen, O.M., Kvalsvold, J., Aarsnes, J.V., 1997. Water impact on a horizontal elastic plate. J. Mar. Sci. Technol. 2, 87–100.

Feng, S., Zhang, G., Wan, D., Jiang, S., Sun, Z., Zong, Z., 2021. On the treatment of hydroelastic slamming by coupling boundary element method and modal superposition method. Appl. Ocean Res. 112, 102595. https://doi.org/10.1016/j.apor.2021.102595

Fontaine, E., Cointe, R., 1992. A second-order solution for the wedge entry with small deadrise angle. In: Proceedings of the Seventh International Workshop on Water Waves and Floating Bodies. Val de Reuil, France, pp. 105–108.

Gilbert, C., Gilbert, J., Javaherian, M.J., 2023. Water entry of a flexible wedge: how flexural rigidity influences spray root and pressure wave propagation. Phys. Rev. Fluids 8 (9), 090502. https://doi.org/10.1103/PhysRevFluids.8.090502

Greenhow, M., 1987. Wedge entry into initially calm water. Appl. Ocean Res. 9 (4), 214–223. https://doi.org/10.1016/0141-1187(87)90003-5

Hascoët, R., Jacques, N., Scolan, Y.-M., Tassin, A., 2019. A two-dimensional analytical model of vertical water entry for asymmetric bodies with flow separation. Appl. Ocean Res. 92, 101878. https://doi.org/10.1016/j.apor.2019.101878

Hirdaris, S.E., Bai, W., Dessi, D., Ergin, A., Gu, X., Hermundstad, O.A., Huijsmans, R., Iijima, K., Nielsen, U.D., Parunov, J., Fonseca, N., Papanikolaou, A., Grygiadis, K., Incecik, A., 2014. Loads for use in the design of ships and offshore structures. Ocean Eng. 78, 131–174. https://doi.org/10.1016/j.oceaneng.2013.09.003

Hosseini, A., Tavakoli, S., Dashtimanesh, A., Mikkola, T., Hirdaris, S., 2024. Drift test analysis of a conventional planing hull utilising CFD and 2d+t models. Ocean Eng. 308, 118226. https://doi.org/10.1016/j.oceaneng.2024.118226

Hosseinzadeh, S., Izadi, M., Tabri, K., 2020. Free fall water entry of a two-dimensional asymmetric wedge in oblique slamming: a numerical study. In: International Conference on Offshore Mechanics and Arctic Engineering. Vol. 84409. American Society of Mechanical Engineers, p. V008T08A013.

Hosseinzadeh, S., Khorasanchi, M., Seif, M.S., 2019. Investigation of planing vessels motion using nonlinear strip theory–an experimental and numerical study. Ships Offshore Struct. 14 (7), 684–697.

Hosseinzadeh, S., Tabri, K., 2021. Hydroelastic effects of slamming impact loads during free-fall water entry. Ships Offshore Struct. 16 (sup1), 68–84.

Hosseinzadeh, S., Tabri, K., 2024. Experimental study on the dynamic response of a 3-d wedge under asymmetric impact. J. Hydrodyn. 36 (2), 263–274.

Hosseinzadeh, S., Tabri, K., Hirdaris, S., Sahk, T., 2023a. Slamming loads and responses on a non-prismatic stiffened aluminium wedge: part i. experimental study. Ocean Eng. 279, 114510.

Hosseinzadeh, S., Tabri, K., Topa, A., Hirdaris, S., 2023b. Slamming loads and responses on a non-prismatic stiffened aluminium wedge: part II. numerical simulations. Ocean Eng. 279, 114309.

Izadi, M., Ghadimi, P., Fadavi, M., Tavakoli, S., 2018a. Hydroelastic analysis of water impact of flexible asymmetric wedge with an oblique speed. Meccanica 53 (10), 2585–2617.

Izadi, M., Ghadimi, P., Fadavi, M., Tavakoli, S., 2018b. Numerical modeling of the freefall of two-dimensional wedge bodies into water surface. J. Brazil. Soc. Mech. Sci. Eng. 40, 1–19. https://doi.org/10.1007/s40430-017-0910-0

Jiao, J., Chen, Z., Xu, S., 2024. Cfd-fem simulation of water entry of aluminium flat stiffened plate structure considering the effects of hydroelasticity. Brodogradnja 75 (1), 75108. . https://brodogradnja.fsb.hr/.

Judge, C., Troesch, A., Perlin, M., 2004. Initial water impact of a wedge at vertical and oblique angles. J. Eng. Math. 48 (3–4), 279–303. https://doi.org/10.1023/B:ENGI.0000018234.40373.13

Jung, S., 2025. Water entry and exit in nature: review. Interface Focus 15 (2), 20240055. https://doi.org/10.1098/rsfs.2024.0055

Kapsenberg, G.K., 2011. Slamming of ships: where are we now? Philos. Trans. R. Soc. A: Math. Phys. Eng. Sci. 369, 2892–2919. https://doi.org/10.1098/rsta.2011.0115

von Kármán, T., 1929. The Impact of Seaplane Floats During Landing. Technical Note 321. National Advisory Committee for Aeronautics (NACA). Washington, DC, USA.

Khabakhpasheva, T.I., Korobkin, A.A., 2013. Elastic wedge impact onto a liquid surface: Wagner's solution and approximate models. J. Fluid. Struct. 36, 32–49. https://doi.org/10.1016/j.jfluidstructs.2012.08.010

Kikuhara, S., 1960. A study of spray generated by seaplane hulls. J. Aero/Space Sci. 415–428.
Kim, J.-H., Kim, Y., Yuck, R.-H., Lee, D.-Y., 2015. Comparison of slamming and whipping loads by fully coupled hydroelastic analysis and experimental measurement. J. Fluid. Struct. 52, 145–165. https://doi.org/10.1016/j.jfluidstructs.2014.10.011
Korobkin, A., 2004. Analytical models of water impact. Eur. J. Appl. Math. 15 (6), 821–838. https://doi.org/10.1017/S0956792504005765
Korobkin, A.A., 2007. Second-order wagner theory of wave impact. J. Eng. Math. 58, 121–139. https://doi.org/10.1007/s10665-006-9094-4
Kvalsvold, J., Faltinsen, O.M., 1993. Hydroelastic modelling of slamming against the wet-deck of a catamaran. In: Proceedings of the 2nd International Conference on Fast Sea Transportation (FAST'93). Japan, pp. 681–697.
Kvalsvold, J., Faltinsen, O.M., 1994. Slamming loads on wet decks of multihull vessels. In: Proceedings of the Second International Conference on Hydroelasticity in Marine Technology. Trondheim, Norway, pp. 205–220.
Lin, Y., Ma, N., Gu, X., Wang, D., 2020. Experimental study on the asymmetric impact loads and hydroelastic responses of a very large container ship. Int. J. Naval Architect. Ocean Eng. 12, 226–240. https://doi.org/10.1016/j.ijnaoe.2019.09.005
Mai, T., Mai, C., Raby, A., Greaves, D.M., 2020. Hydroelasticity effects on water-structure impacts. Exp. Fluids 61, 1–19. https://doi.org/10.1007/s00348-020-2966-6
Maki, K.J., Lee, D., Troesch, A.W., Vlahopoulos, N., 2011. Hydroelastic impact of a wedge-shaped body. Ocean Eng. 38 (4), 621–629.
Meyerhoff, W.K., 1965. Die berechnung hydroelastischer stösse. Schiffstechnik 12 (60), 18–30.
Moradi, H., Rahbar Ranji, A., Haddadpour, H., Moghadas, H., 2021. A hybrid model for simulation of fluid-structure interaction in water entry problems. Phys.Fluids 33 (1), 017102. https://doi.org/10.1063/5.0034200
OpenFOAM Wiki contributors, 2016. Installation/linux/foam-extend-4.1. https://openfoamwiki.net/index.php/Installation/Linux/foam-extend-4.1. Accessed: 2025-09-20.
Panciroli, R., Shams, A., Porfiri, M., 2015. Experiments on the water entry of curved wedges: high speed imaging and particle image velocimetry. Ocean Eng. 94, 213–222. https://doi.org/10.1016/j.oceaneng.2014.12.004
Peddamallu, P., Rajendran, S., Saripilli, J., Zhou, X., 2025. Coupling a time-domain code with a RANS solver for slamming analysis. Ships Offshore Struct. 20 (Issue 11), 1731–1744. https://doi.org/10.1080/17445302.2024.2397887
Peseux, B., Gornet, L., Donguy, B., 2005. Hydrodynamic impact: numerical and experimental investigations. J. Fluid. Struct. 21 (3), 277–303. https://doi.org/10.1016/j.jfluidstructs.2005.05.003
Piro, D.J., Maki, K.J., 2013. Hydroelastic analysis of bodies that enter and exit water. J. Fluids Struct. 37, 134–150.
Povitsky, A.S., 1935. Seaplane Landing Impact. Technical Report Report No. 199. Central Aero-Hydrodynamical Institute. Moscow.
Scolan, Y.-M., Korobkin, A.A., 2001. Three-dimensional theory of water impact. part 1. inverse wagner problem. J. Fluid Mech. 440, 293–326. https://doi.org/10.1017/S002211200100475X
Semenov, Y.A., Iafrati, A., 2006. On the nonlinear water entry problem of asymmetric wedges. J. Fluid Mech. 547, 231–256. https://doi.org/10.1017/S0022112005007329
Shi, X., Qu, Q., Liu, P., Hu, T., Zheng, Y., Zhou, P., 2025. Morphology of entrapped air bubbles during water impact of a flat plate. Phys. Rev. Fluids 10, 024803. https://doi.org/10.1103/PhysRevFluids.10.024803
Silva, M.L., Ravichandran, G., 2012. Stress field evolution under mechanically simulated hull slamming conditions. Exp. Mech. 52 (1), 107–116. https://doi.org/10.1007/s11340-011-9502-5
Spalding, D.B., 1972. A novel finite difference formulation for differential expressions involving both first and second derivatives. Int. J. Numer. Method. Eng. 4 (4), 551–559. https://doi.org/10.1002/nme.1620040409
Stenius, I., Rosén, A., Battley, M., Allen, T., 2013. Experimental hydroelastic characterization of slamming loaded marine panels. Ocean Eng. 74, 1–15. https://doi.org/10.1016/j.oceaneng.2013.09.007
Stenius, I., Rosén, A., Kuttenkeuler, J., 2007. Explicit FE-modelling of hydroelasticity in panel-water impacts. Int. Shipbuild. Progr. 54 (2–3), 111–127.
Sun, S.-L., Chen, Y.-H., Hu, J., Xu, W.-J., Yang, H., 2020. Fully nonlinear investigation on water entry of a rigid paraboloid. Eng. Anal. Bound. Element. 117, 57–65. https://doi.org/10.1016/j.enganabound.2020.03.018
Sun, S.-L., Sun, J.-Y., Wang, S., Li, Y.-H., Ren, H.-L., 2024. Fluid-structure interaction analysis of curved wedges entering into water. Phys. Fluids 36 (10), 102121. https://doi.org/10.1063/5.0235583
Tavakoli, S., Babanin, A.V., Hirdaris, S., 2023a. Hydroelastic analysis of hard chine sections entering water-observations for use in preliminary design stage. J. Offshore Mech. Arctic Eng. 145 (5), 051901. https://doi.org/10.1115/1.4063026
Tavakoli, S., Bliandi, R.N., Mancini, S., De Luca, F., Dashtimanesh, A., 2020. Dynamic of a planing hull in regular waves: comparison of experimental, numerical and mathematical methods. Ocean Eng. 217, 107959. https://doi.org/10.1016/j.oceaneng.2020.107959
Tavakoli, S., Dashtimanesh, A., 2019. A six-DOF theoretical model for steady turning maneuver of a planing hull. Ocean Eng. 189, 106328. https://doi.org/10.1016/j.oceaneng.2019.106328
Tavakoli, S., Mikkola, T., Hirdaris, S., 2023b. A fluid-solid momentum exchange method for the prediction of hydroelastic responses of flexible water entry problems. J. Fluid Mech. 965, A19. https://doi.org/10.1017/jfm.2023.386
Tavakoli, S., Niazmand Bilandi, R., Mancini, S., Kirezci, C., 2026. Nonlinear motions and dynamic intermittency of planing hulls in random wave fields: a structure-function approach. Ocean Eng. 343, 123467. https://doi.org/10.1016/j.oceaneng.2025.123467
Tavakoli, S., Singh, M., Hosseinzadeh, S., Hu, Z., Shao, Y., Wang, S., Huang, L., Grammatikopoulos, A., Li, Y.P., Khojasteh, D., Liu, J., Dolatshah, A., Cheng, H., Hirdaris, S., 2025. A review of flexible fluid-structure interactions in the ocean: progress, challenges, and future directions. Ocean Eng. 342, 122545. https://doi.org/10.1016/j.oceaneng.2025.122545
Tsaousis, T.D., Papadopoulos, P.K., Chatjigeorgiou, I.K., 2020. A semi-analytical solution for the three-dimensional wagner steep wave impact on a vertical circular cylinder. Appl. Math. Modell. 77, 902–921. https://doi.org/10.1016/j.apm.2019.08.028
Tuković, Ž., Karač, A., Jasak, H., Cardiff, P., Ivanković, A., 2018. OpenFOAM finite volume solver for fluid-solid interaction. Trans. FAMENA 42 (3), 1–31. https://doi.org/10.21278/TOF.42301
Underwood, J., Alley, E., Andric, J., Boote, D., Gao, Z., Van Hoeve, A., Jelovica, J., Kawamura, Y., Kim, Y., Liu, J., et al., 2022. Committee II. 1: quasi-static response. In: International Ship and Offshore Structures Congress. SNAME, p. D011S001R004.
Vasin, A.D., 1993. Hydroelastic interaction of a wedge-shaped construction entering a liquid. Fluid Dyn. 28 (3), 387–392. https://doi.org/10.1007/BF01062136
Vijith, P.P., Rajendran, S., 2023. Hydroelastic effects on the vertical bending moment of a container ship in head and oblique seas. Ocean Eng. 285, 115385. https://doi.org/10.1016/j.oceaneng.2023.115385
van der Vorst, H.A., 1992. Bi-CGSTAB: a fast and smoothly converging variant of bi-CG for the solution of nonsymmetric linear systems. SIAM J. Sci. Stat. Comput. 13 (2), 631–644. https://doi.org/10.1137/0913035
Wagner, H., 1932. Über stoß- und gleitvorgänge an der oberfläche von flüssigkeiten. Zeitschrift für Angewandte Mathematik und Mechanik 12, 193–215.
Wang, S., Karmakar, D., Soares, C.G., 2016. Hydroelastic impact of a horizontal floating plate with forward speed. J. Fluids Struct. 60, 97–113. https://doi.org/10.1016/j.jfluidstructs.2015.11.005
Wang, S., Soares, C.G., 2017. Review of ship slamming loads and responses. J. Mar. Sci. Appl. 16, 427–445. https://doi.org/10.1007/s11804-017-1437-3
Wang, S., Xiang, G., Soares, C.G., 2021. Assessment of three-dimensional effects on slamming load predictions using openFOAM. Appl. Ocean Res. 112, 102646. https://doi.org/10.1016/j.apor.2021.102646
Watanabe, I., 1986. Analytical expression of hydrodynamic impact pressure by matched asymptotic expansion technique. Trans. West Japan Soc. Naval Architects 71, 77–85.
Weining, F., 1936. Berücksichtigung der elastizität beim aufschlag eines gekielten flugzeugschwimmers auf das wasser (ebenes problem). Luftfahrtforschung 13, 155–159.
Wilson, S.K., 1989. The Mathematics of Ship Slamming. D. phil. thesis. University of Oxford.
Xiang, G., Wang, S., Soares, C.G., 2020. Study on the motion of a freely falling horizontal cylinder into water using openFOAM. Ocean Eng. 195, 106811. https://doi.org/10.1016/j.oceaneng.2019.106811
Xu, L., Troesch, A.W., Vorus, W.S., 1998. Asymmetric vessel impact and planing hydrodynamics. J. Ship Res. 42 (3), 187–198.
Yan, D., Hosseinzadeh, S., Lakshmynarayanana, A., Mikkola, T., Hirdaris, S., 2021. Comparative study on numerical hydroelastic analysis of impact-induced loads. In: Of the 23rd Numerical Towing Tank Symposium, p. 6.
Yan, D., Mikkola, T., Kujala, P., Hirdaris, S., 2023. Hydroelastic analysis of slamming induced impact on stiff and flexible structures by two-way CFD-FEA coupling. Ships Offshore Struct. 18 (9), 1300–1312. https://doi.org/10.1080/17445302.2022.2116231
Yan, D., Mikkola, T., Lakshmynarayanan, A., Tödter, S., Schellin, T.E., Neugebauer, J., Moctar, O.e., Hirdaris, S., 2022. A study into the FSI modelling of flat plate water entry and related uncertainties. Mar. Struct. 86, 103296. https://doi.org/10.1016/j.marstruc.2022.103296
Yettou, E.-M., Desrochers, A., Champoux, Y., 2006. Experimental study on the water impact of a symmetrical wedge. Fluid Dyn. Res. 38 (1), 47–66. https://doi.org/10.1016/j.fluiddyn.2005.09.003
Zarnick, E.E., 1978. A Nonlinear Mathematical Model of Motions of a Planing Boat in Regular Waves. Technical Report. David W. Taylor Naval Ship Research and Development Center. Bethesda, MD, USA.
Zhao, R., Faltinsen, O.M., 1993. Water entry of two-dimensional bodies. J. Fluid Mech. 246, 593–612. https://doi.org/10.1017/S0022112093000360
Zhao, R., Faltinsen, O.M., Aarnes, J., 1996. Water entry of arbitrary two-dimensional sections with and without flow separation. In: Proceedings of the 21st International Symposium on Naval Hydrodynamics. Trondheim, Norway, pp. 118–132.